micelle with sFlt-1 pDNA is interesting and worthy to develop further for antiangiogenic gene therapy of solid tumors.

Acknowledgment. This work was financially supported in part by the Core Research Program for Evolutional Science and Technology (CREST) from Japan Science and Technology Agency (JST) as well as by Grants-in-Aid for Young Scientists (A) and Exploratory Research. We express our appreciation to Masabumi Shibuya (Tokyo Medical and Dental University) for providing pVL 1393 baculovirus vector pDNA encoding human sFlt-1. We thank Kazuhiro Aoyagi, Yoko Hasegawa, Kotoe Date, and Satomi Ogura (The University of Tokyo) for technical assistance.

Supporting Information Available: Synthesis of thiolated block copolymer and Supporting Figures 1, 2, 3, and 4. This material is available free of charge via the Internet at http://pubs.acs.org.

MP9002317

NANOMEDICINE

Journal of Controlled Release 140 (2009) 306–311

Contents lists available at ScienceDirect

Journal of Controlled Release

journal homepage: www.elsevier.com/locate/jconrel

Enhanced magnetic resonance imaging of experimental pancreatic tumor *in vivo* by block copolymer-coated magnetite nanoparticles with TGF-β inhibitor

Michiaki Kumagai [a,e,1], Mitsunobu R. Kano [b,f,1], Yasuyuki Morishita [b], Motomi Ota [a], Yutaka Imai [a], Nobuhiro Nishiyama [a,e,f], Masaki Sekino [c], Shoogo Ueno [d], Kohei Miyazono [b,f], Kazunori Kataoka [a,e,f,*]

[a] Department of Materials Engineering, Graduate School of Engineering, The University of Tokyo, 7-3-1 Hongo, Bunkyo-ku, Tokyo 113-8656, Japan
[b] Department of Molecular Pathology, Graduate School of Medicine, The University of Tokyo, 7-3-1 Hongo, Bunkyo-ku Tokyo 113-0033, Japan
[c] Department of Advanced Energy, Graduate School of Frontier Sciences, The University of Tokyo, 5-1-5, Kashiwanoha, Kashiwa-shi, Chiba, 277-8561, Japan
[d] Department of Applied Quantum Physics, Graduate School of Engineering, Kyushu University, 6-10-1 Hakozaki, Higashi-ku Fukuoka 812-8581, Japan
[e] Center for Disease Biology and Integrative Medicine, School of Medicine, The University of Tokyo, 7-3-1 Hongo, Bunkyo-ku, Tokyo 113-0033, Japan
[f] Center for NanoBio Integration, The University of Tokyo, 7-3-1 Hongo, Bunkyo-ku, Tokyo 113-8656, Japan

ARTICLE INFO

Article history:
Received 13 March 2009
Accepted 5 June 2009
Available online 12 June 2009

Keyword:
Magnetic resonance imaging
Pancreatic cancer
TGF-β
Magnetite nanoparticles
Poly(ethylene glycol)

ABSTRACT

Early detection of solid tumors, particularly pancreatic cancer, is of substantial importance in clinics. Enhanced magnetic resonance imaging (MRI) with iron oxide nanoparticles is an available way to detect the cancer. The effective and selective accumulation of these nanoparticles in the tumor tissue is needed for improved imaging, and in this regard, their longevity in the blood circulation time is crucial. We developed here block copolymer-coated magnetite nanoparticles for pancreatic cancer imaging, by means of a chelation between the carboxylic acid groups in poly(ethylene glycol)–poly(aspartic acid) block copolymer (PEG–PAsp) and Fe on the surface of the iron oxide nanoparticles. These nanoparticles had considerably narrow distribution, even upon increased ionic strength or in the presence of fetal bovine serum. The PEG–PAsp-coated nanoparticles were further shown to be potent as a contrast agent for enhanced MRI for an experimental pancreatic cancer, xenografts of the human-derived BxPC3 cell line in BALB/c nude mice, with combined administration of TGF-β inhibitor. Iron staining of tumor tissue confirmed the accumulation of the nanoparticles in tumor tissue. Use of the PEG–PAsp-coated magnetite nanoparticles, combined with the TGF-β inhibitor, is of promising clinical importance for the detection of intractable solid cancers, including pancreatic cancer.

1. Introduction

Pancreatic cancer, one of the intractable solid tumors, is the fourth leading cause of cancer-related deaths in the United States and the fifth in Japan [1]. The average survival period of patients suffering from advanced pancreatic adenocarcinoma is still extremely short, only 6 months, despite recent progress in the chemotherapies [2]. Although cancer detection and treatment have been greatly improved through the development of diagnostic imaging modalities, it is still difficult to detect pancreatic cancer [3]. Consequently, the development of diagnostic systems to detect these cancers is of great importance.

Recently, superparamagnetic iron oxide (SPIO) nanoparticles composed of either magnetite (Fe_3O_4) or maghemite (g-Fe_2O_3) have been studied as contrast agents for magnetic resonance (MR) imaging [4]. Commercial application for human diagnosis based on SPIO particles is currently available. However, since cancer detection requires the systemic administration of iron oxide nanoparticles, the circulation time of the particles must be prolonged. Several studies have already reported that the behavior of magnetic nanoparticles in the bloodstream depends closely on their nanoscale morphology, including overall diameter, size distribution, or nature of the surface [5,6]. Additionally, the surface modification of iron oxide nanoparticles has proved a versatile strategy for improving their biological performance, including the reduction of immunogenicity and enhancement of targeted delivery to specific tissues [7]. However, the overall correlation between the surface modification of nanoparticles and their *in vivo* behavior remains to be further elucidated.

Various methods of stabilization for SPIO nanoparticles have been reported to date [8]. One of the most feasible approaches could be the stabilization of SPIO by coated with biocompatible polymers [9]. Suitable polymers, including poly(ethylene glycol) (PEG) and its block copolymers, are promising for the development of SPIO systems with defined surface properties. This coating of particles with PEG, or PEGylation, to avoid their uptake by the reticuloendothelial system, is under intensive investigation. We also previously reported the accumulation of β-FeOOH nanoparticles coated with PEG–poly(α,β-aspartic acid) block copolymer

* Corresponding author. Department of Materials Engineering, Graduate School of Engineering, The University of Tokyo, 7-3-1 Hongo, Bunkyo-ku, Tokyo 113-8656, Japan.
E-mail address: kataoka@bmw.t.u-tokyo.ac.jp (K. Kataoka).
[1] Equal contribution.

0168-3659/$ – see front matter © 2009 Elsevier B.V. All rights reserved.
doi: 10.1016/j.jconrel.2009.06.002

(PEG–PAsp) into experimental colon adenocarcinoma, which could be applicable for tumor-selective MR imaging [10]. The multivalent bonding of PEG-based block copolymer to magnetic nanoparticles may thus help to facilitate the accumulation of these nanoparticles into some solid tumors. However, magnetic nanoparticles of any design have not yet been successful in exhibiting sufficient accumulation in intractable solid cancers, including pancreatic adenocarcinoma [1]. In addition to improving the performance of iron-based contrast agents (e.g. biocompatibility), the co-administration of adjuvant small molecules could increase the accumulation of these agents in target cancer tissue. In fact, we have recently shown that the administration of the small molecule TGF-β inhibitor (LY364947) at a low dose [11], which could minimize the potential side effects of the TGF-β inhibitor, can alter the tumor microenvironment and enhance the EPR effect in these cancers [12]. Therefore, the combined use of TGF-β inhibitor could be promising to diagnose intractable cancers with a long-circulating MRI contrast agent. Here, we demonstrated the successful MR imaging of experimental pancreatic cancer by the systemic administration of newly developed SPIO nanoparticles coated by PEG–PAsp in aid of TGF-β inhibitor.

2. Materials and methods

2.1. Reagents

β-benzyl L-aspartate and bis(trichloromethyl)carbonate (triphosgene) were purchased from Sigma-Aldrich Corporation (St. Louis, MO, USA) and Tokyo Chemical Industry Co., Ltd. (Tokyo, Japan), respectively. α-Methoxy-ω-amino-poly(ethylene glycol) (CH_3O–PEG–NH_2; $M_w = 12000$) was purchased from NOF Corporation (Tokyo, Japan). Tetrahydrofuran (THF), *n*-hexane, *N,N*-dimethylformamide (DMF), CH_2Cl_2 were doubly-distilled according to the standard procedures. The magnetite nanoparticles were supplied by Toda Kogyo Corporation (Hiroshima, Japan; average particle size of magnetite: 10 nm). Resovist® was obtained from Bayer HealthCare Co., Ltd. (Osaka, Japan). TGF-β inhibitor was purchased from EMD Chemicals Inc. (San Diego, CA, USA) (LY364947; catalog no. 616451).

2.2. Synthesis of poly(ethylene glycol)–poly(α,β-aspartic acid) block copolymer (PEG–PAsp)

PEG–PAsp was synthesized by a previously reported procedure [13]. Briefly, poly (ethylene glycol)–*b*–poly(β-benzyl L-aspartate) block copolymer (PEG–PBLA) was prepared by ring-opening polymerization of N-carboxy anhydride of β-benzyl L-aspartate (BLA-NCA) from the ω-NH_2 group of PEG ($M_w = 1.2 \times 10^4$). Molecular weight distribution of PEG–PBLA was narrow as $M_w/M_n = 1.06$, which was determined by gel permeation chromatography [columns: TSK-gel G3000HHR, G4000HHR (Tosoh, Yamaguchi, Japan); eluent: DMF containing 10 mM LiCl; flow rate: 0.8 ml/min; detector: refractive index (RI); temperature: 40 °C]. The composition of these block copolymers was determined by ^{1}H NMR from peak intensity ratios of methylene protons of PEG (OCH_2CH_2: $d = 3.7$ ppm) and phenyl protons of the β-benzyl groups of PBLA ($-CH_2C_6H_5$: $d = 7.3$ ppm). The polymerization degree of BLA in block copolymer was calculated to be 38. The benzyl groups of PEG–PBLA were then removed by alkaline hydrolysis using 0.1 N NaOH to obtain PEG–PAsp as follows:

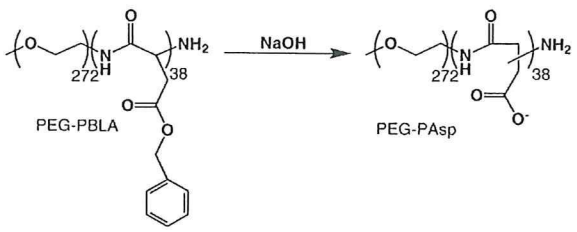

2.3. Preparation of PEG–PAsp-coated magnetite nanoparticles

PEG–PAsp-coated magnetite nanoparticles were prepared according to the previous method with slight modification [10]. Briefly, magnetite solution was quickly added to an aqueous solution of PEG–PAsp with varying feed molar ratios of aspartic acid residues to Fe ([Asp]/[Fe]) in the range of 0.01 to 1. The final concentration of magnetite was adjusted to 10 mmol/l. The mixed solutions were incubated at room temperature for 24 h to obtain magnetite nanoparticles coated with PEG–PAsp. Purification of the PEG–PAsp-coated magnetite nanoparticles was carried out by ultrafiltration (MWCO 200 000; polysulfone membrane, Toyo Roshi Co. Ltd., Tokyo, Japan).

2.4. Physicochemical characterization of the nanoparticles

The morphology and size distribution of the nanoparticles were examined by transmission electron microscopy (H-7000, Hitachi, Ltd., Tokyo, Japan) at an accelerating voltage of 75 kV. The TEM samples were prepared by mounting a drop of aqueous iron oxide nanoparticles suspension on carbon-coated 400 mesh Cu grids and allowing them to dry in air. Fourier transform infrared (FT-IR) spectra were obtained using a FT-IR spectrophotometer (FT/IR615, JASCO Corporation, Hachioji, Tokyo, Japan) with a resolution of 4 cm^{-1}. To characterize the interaction between block copolymer and magnetite nanoparticles, a small amount of nanoparticles powder was milled with KBr, and then pressed into a disc for analysis. Each spectrum was scanned 64 times to increase the signal-to-noise ratio. The Fe content in the nanoparticles was determined by ion coupled plasma-mass spectroscopy (ICP-MS, 4500, Hewlett Packard, Palo Alto, CA, USA). The amount of adsorbed block copolymer on magnetite nanoparticles was measured by thermogravimetric analysis (TGA) (EXSTAR6200 TG/DTA, Seiko Instruments Inc., Chiba, Japan) in nitrogen atmosphere with a heating rate of 10 °C/min in the temperature range of 25–1100 °C.

2.5. Light scattering and ζ-potential measurements

The size distribution of the PEG–PAsp-coated magnetite nanoparticles was examined by dynamic light scattering (DLS) DLS-7000 (Otsuka Electronics Co., Ltd., Osaka, Japan). Vertically polarized light with a wavelength of 488 nm from an Ar-ion laser (15 mW) was used as the incident beam. All measurements were conducted at 37 °C, and the data were analyzed by the cumulant method to determine the hydrodynamic diameters of the particles. The ζ-potential of PEG–PAsp-coated magnetite nanoparticles at 37 °C was measured by a Zetasizer NanoZS instrument equipped with a DTS5001 cell (Malvern Instruments Ltd., Worcestershire, UK).

2.6. Characterization of the r_2 relaxivities

The MR contrast effect of the magnetite nanoparticles was examined by measuring their proton relaxivities, r_2, of which the definition is the slope of the concentration dependence given as:

$$1/T_2 = 1/T_2(0) + r_2[\mathrm{Fe}]$$

Thus, a plot of $1/T_2$ versus concentration gives the relaxivity as the slope, where T_2 is the transversal relaxation time, $1/T_2$ is the transversal relaxation rate constant in the presence of a paramagnetic species, and $1/T_2(0)$ is the transversal relaxation rate constant in the absence of a paramagnetic species. The magnetite nanoparticles were dispersed into deionized water at concentrations of 0.5, 1.0, 1.5, 2.0, and 2.5 mM and the T_2 of these nanoparticle solutions was measured at 25 °C in water with a 0.47 T minispectrometer (Minispec, Bruker

Optics Inc., Woodlands, TX, USA) using the Carr–Purcell–Meiboom–Gill (CPMG) method [14].

2.7. In vivo MR imaging

The BxPC3 human pancreatic adenocarcinoma cell line was obtained from the American Type Culture Collection (Manassas, VA, USA). The BxPC3 cells were grown in RPMI 1640 medium supplemented with 10% FBS. BALB/c nude mice (female, 5–6 weeks of age), obtained from Charles River Laboratories Japan Inc. (Tokyo, Japan), were inoculated subcutaneously with BxPC3 cells (1×10^7 cells/mouse). After 3–4 weeks, MR imaging of the tumors was conducted with a 4.7 T scanner (INOVA200, Varian, Inc., Palo Alto, CA, USA). Twenty-four hours prior to the *in vivo* MR imaging, animals were treated with TGF-β inhibitor, 5 mg/ml in 4 μl of DMSO and diluted by 100 μl of PBS, at 1 mg/kg by intraperitoneal injection. Subsequently, the mice were injected at a dose of 0.1 mmolFe/kg, with Resovist® or PEG–PAsp-coated magnetite nanoparticles. A total of 4 conditions ($n=5$ mice each) were investigated, i.e. with or without TGF-β inhibitor for both Resovist® or PEG–PAsp-coated magnetite nanoparticles. Imaging was performed at different temporal points (e.g., preinjection, 1 h postinjection, and 2 h postinjection). For the T_2-weighted MR imaging of live mice, the following parameters were adopted: spin-echo method, point resolution = 234×234 μm, section thickness = 2.0 mm, TE = 60 ms, TR = 3000 ms, number of acquisitions = 5. All animals were treated in accordance with the guidelines of the Animal Ethics Committee of the University of Tokyo.

2.8. Histology

The excised samples were fixed overnight in 4% paraformaldehyde and then paraffin-embedded. Embedded samples were thin sliced at 10 μm thick and then stained using an Iron Stain Kit (Muto Pure Chemicals Co., Ltd., Tokyo, Japan), based on McFadzean's protocol [15], with nuclear post-staining by 1% Safranin O. Iron staining was observed using an AX80 microscope (Olympus Corporation, Tokyo, Japan). The photographs were further quantified using Adobe Photoshop software (Adobe Systems Incorporated, San Jose, CA, USA), ImageJ software (National Institute of Health, MD, USA), and Microsoft Excel software (Microsoft Corporation, Redmond, WA, USA).

3. Results and discussion

3.1. The physicochemical properties of the PEG–PAsp-coated magnetite nanoparticle: diameter and surface polymer density

For solid tumor diagnosis, it is important to develop well-designed magnetite nanoparticles. The key physicochemical properties of magnetite nanoparticles are size, surface polymer density, and surface charge, since these characteristics can affect accumulation of magnetite nanoparticles to solid tumor. The PEG–PAsp-coated magnetite nanoparticles were prepared by mixing solutions of magnetite nanoparticles and PEG–PAsp with various molar ratios of the Asp residues to Fe (Asp/Fe); Asp/Fe ranged from 0.01 to 0.5, where [Fe] = 10 mmol/l. As seen in Fig. 1, the transmission electron microscopy (TEM) image with 75 kV accelerating voltage of nanoparticles mounted on carbon grid from aqueous solution revealed that PEG–PAsp-coated magnetite nanoparticles take a cubic shape with a mean particle diameter of approximately 10 nm. The PEG–PAsp coating was observed as a layer with a thickness of approximately 5 nm, surrounding the magnetite nanoparticles. It was also observed in the TEM image that these PEG–PAsp-coated nanoparticles form clusters with a size range of 100 nm.

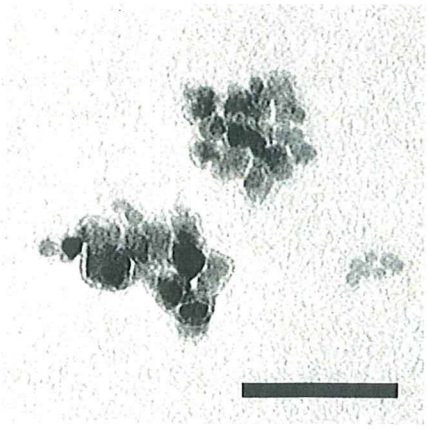

Fig. 1. TEM image of the PEG–PAsp-coated magnetite nanoparticles. Bar: 100 nm.

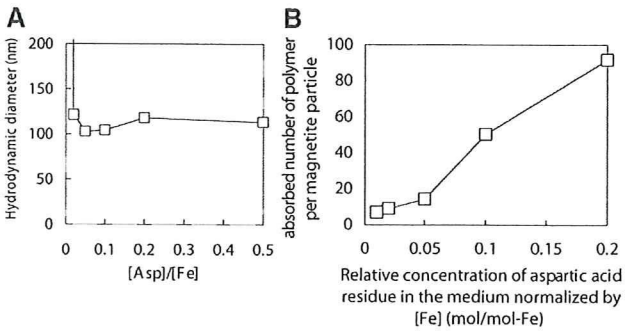

Fig. 2. Physicochemical properties of the PEG–PAsp-coated magnetite nanoparticles. (A) Hydrodynamic diameter vs. relative concentration of aspartic acid residue in the medium normalized by [Fe] (mol/mol-Fe) (=[Asp]/[Fe]), and (B) Change in the adsorbed density of PEG–PAsp on the magnetite surface estimated from TGA analysis with a bulk concentration of PEG–PAsp. Temperature = 37 °C; medium: distilled water.

The hydrodynamic diameter of these nanoparticles in aqueous medium was then measured with DLS and shown to be in the range of 100 to 120 nm with unimodal distribution, for Asp/Fe ratios ranging from 0.02–0.5. This DLS data is consistent with the cluster formation of nanoparticles indicated from TEM images. However, with a lowered Asp/Fe ratio as 0.01, the hydrodynamic diameter increased significantly (Fig. 2A). This result indicates that there is a critical surface concentration of PEG to effectively prevent the PEG–PAsp-coated magnetite nanoparticles from the agglomeration. The purified nanoparticles were stable in distilled water as 100 nm-scaled cluster at room temperature as well as at 37 °C, maintaining the initial photon count and distribution in DLS analysis for at least one month, even after the ultrafiltration to remove free PEG–PAsp possibly remained in the reactant.

The density of the PEG–PAsp block copolymer on the magnetite particle surface was estimated by TGA. Here, nanoparticles were heated in the nitrogen atmosphere to selectively vaporize the polymer fraction. Eventually, the amount of absorbed polymer on the surface of the nanoparticles was measured from the weight change by heating. The polymer density was then calculated from the TGA measurement for all the nanoparticles, assuming the cubic morphology as evidenced by microscopy and a density of 5.05 g/cm^3 for magnetite. As seen in Fig. 2B, the number of polymer strands on the nanoparticle surface was as high as 100. This data suggests that the PEG density on the magnetite nanoparticles is a little lower than that of PEGylated gold nanoparticles prepared through the surface tethering of PEG-SH [16].

3.2. The mechanism of PEG–PAsp adsorption on the magnetite nanoparticles

To confirm the formation of PEG–PAsp coating on the magnetite nanoparticles, the ζ-potential of bare and PEG–PAsp-coated magnetite nanoparticles was measured in 10 mM MOPS buffer as a function of

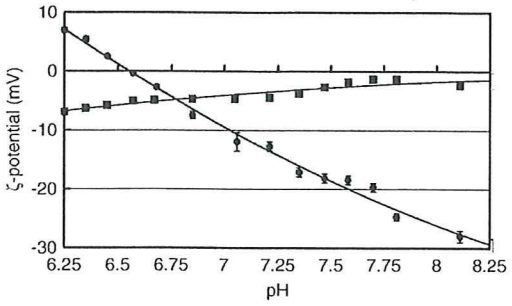

Fig. 3. Change in the ζ-potential with pH for bare (●) and PEG–PAsp-coated (■) magnetite nanoparticles. Temperature = 37 °C; medium: 10 mM MOPS buffer.

pH (Fig. 3). The isoelectric point (IEP) of the bare magnetite nanoparticles was estimated as approximately 6.6, which is consistent with the reported IEP value of iron oxide [17]. In a lower pH (below the IEP), the magnetite nanoparticle surface was protonated to result in a positive ζ-potential. Thus, in this pH range, electrostatic attraction between positively-charged magnetite nanoparticles and negatively charged PEG–PAsp is expected to occur, allowing the PEG–PAsp adsorption to the nanoparticle surface. Alternatively, the bare magnetite nanoparticles possess negative ζ-potential at physiological pH 7.4, whereas the ζ-potential shifted to the neutral value for PEG–PAsp modified nanoparticles in 10 mM MOPS buffer (pH 7.4), being consistent with the formation of a PEG shell layer. Also, these data suggest that there should be an adsorption mechanism other than simple electrostatic interaction, because magnetite has a negative ζ-potential value at pH 7.4 to induce electrostatic repulsive force against negatively charged carboxylates in PEG–PAsp. The adsorption mechanism under physiological pH was suggested to be the monodentate chelation (I) (Fig. 4) from the result of Fourier transform infrared spectroscopy [18], as explained in detail in Supplemental Text with Supplemental Fig. 1 and Supplemental Table 1.

3.3. Comparison study of the physicochemical characteristics of the PEG–PAsp- and dextran-coated magnetite nanoparticles

The MRI detection limit was compared between the PEG–PAsp- and dextran-coated magnetite nanoparticles in the field of 0.47 T at 25 °C from the relaxivity r_2, exhibiting the sensitivity of the T_2 MRI contrast agent. The dextran-coated magnetite used in this study was the one already in clinical use, Resovist®. Eventually, the relaxivity r_2 of the PEG–PAsp nanoparticle was calculated to be 138 $mM^{-1}\,s^{-1}$, the value similar to Resovist® [19].

The hydrodynamic diameter observed between the PEG–PAsp-coated and dextran-coated magnetite nanoparticles differed significantly in an NaCl-concentration-dependent manner (Fig. 5A). Although the hydrodynamic diameter of the PEG–PAsp-coated magnetite nanoparticles did not change significantly up to 3 M NaCl, indicating the appreciable stability of the PEG–PAsp-coating, that of Resovist® significantly increased even at NaCl = 0.15 M, and reached more than 1 μm at NaCl = 0.5 M, due to the drastic aggregation. Note that the PEG–PAsp-coated nanoparticles did not show any change in

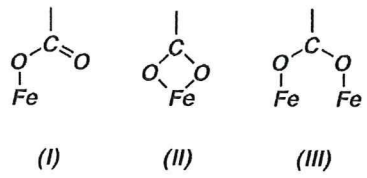

Fig. 4. Modes of carboxylate-metal complexation: monodentate (**I**), bidentate chelating (**II**), and bidentate bridging (**III**).

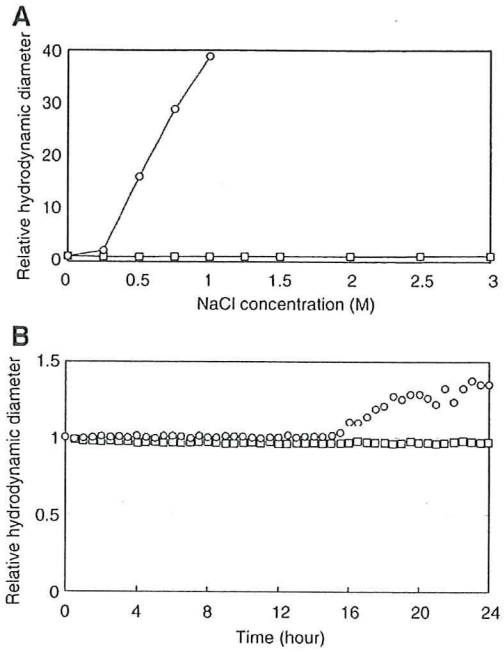

Fig. 5. NaCl concentration (A) and time (B) dependencies of the relative hydrodynamic diameter of magnetite nanoparticles, □: PEG–PAsp-coated nanoparticles, ○: dextran-coated nanoparticles (Resovist®). Fe concentration = 2 mmol/l; temperature = 37 °C; medium 10 mM Tris–HCl buffered saline (pH 7.4). 10% fetal bovine serum was contained in (B).

their size even after one month storage in 10 mM Tris–HCl buffered saline (pH 7.4, 37 °C) (data not shown).

The colloidal stability of the PEG–PAsp-coated magnetite nanoparticles in physiological conditions was also examined. We incubated them in 10 mM Tris–HCl buffered saline (pH 7.4) containing 10% fetal bovine serum at 37 °C for 24 h and measured the change of the hydrodynamic diameter (Fig. 5B). The size of the PEG–PAsp-coated magnetite nanoparticles did not obviously change during the 24-hour storage time. On the other hand, the size of Resovist® increased by the formation of aggregates after 16 h of storage time.

The stability of the PEG–PAsp-coated nanoparticles may come from the multivalent bonding between flanking carboxylic groups and the magnetite surface, as suggested by FT-IR study. These findings are consistent with a report showing that PEG-oligo(aspartic acid) block copolymer-coated iron oxide nanoparticles were stable at pH 2–11 and in 1 M NaCl, where the repeating number of aspartic acid units was 3 or more [20]. In contrast, instability of Resovist® against salt addition may be due to weak interaction between magnetite and hydroxyl groups of dextran [21].

3.4. MR imaging of experimental pancreatic cancer in vivo

The MR imaging of tumor tissue *in vivo* was then conducted by comparing PEG–PAsp- and dextran-coated magnetite nanoparticles, Resovist®. Resovist® has already been approved for clinical use as a liver-specific MRI contrast agent, due to accumulation into the reticuloendothelial system (RES) of the normal liver. Most malignant liver tumors do not contain RES cells and therefore are contrasted positive by Resovist®. A xenografted BxPC3 human pancreatic adenocarcinoma cell line in nude mice, characterized histologically by fibrosis and hypovascularity, was used as a model of intractable cancer. Recently, we reported that the administration of TGF-β inhibitor to tumor model mice significantly enhanced the intratumoral accumulation of nanoparticles encapsulating anticancer drugs [11]. Thus, we tested the effect of the i.p. administration of TGF-β

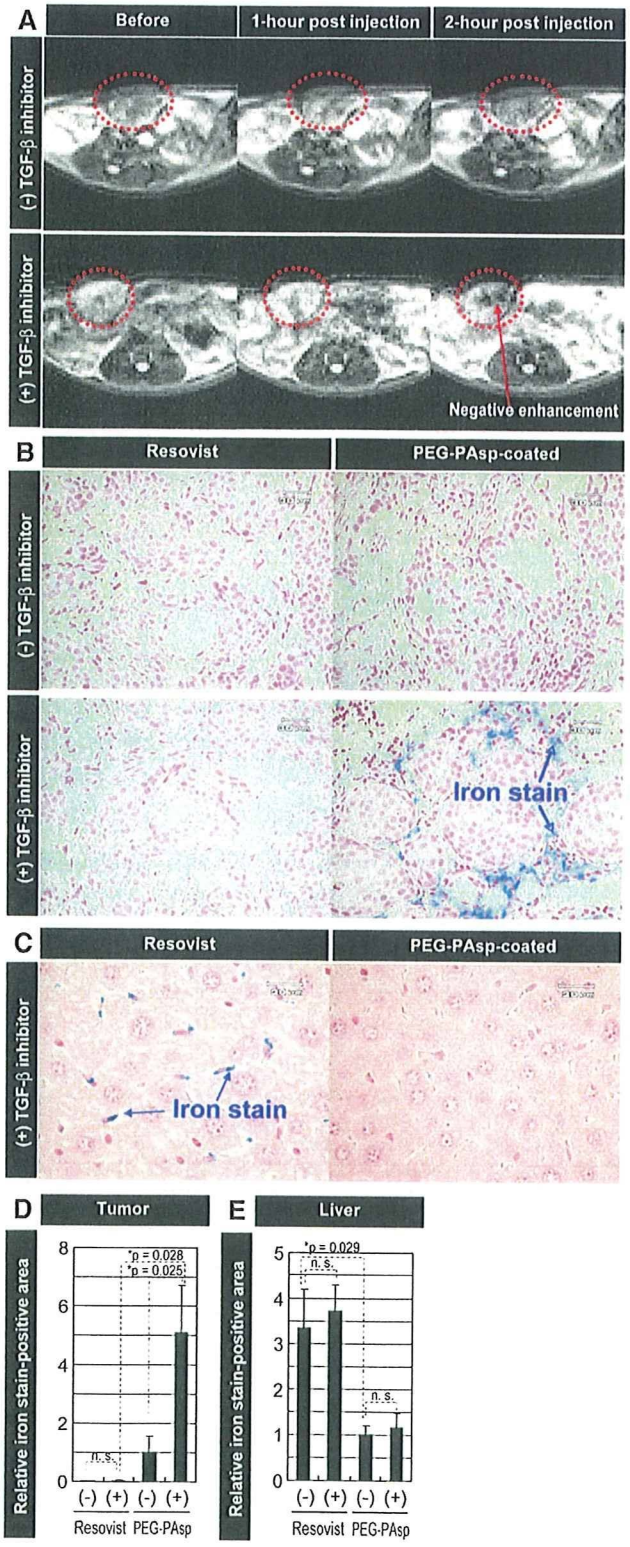

Fig. 6. MR imaging of experimental pancreatic cancer *in vivo* and the distribution of the nanoparticles in cancer and liver tissues. (A) T_2-weighted images of tumor-implanted mice (tumor sites are circled by red dotted line) at different temporal points after injection of PEG–PAsp-coated magnetite nanoparticles and TGF-β inhibitor. All images were obtained in a field strength of 4.7 T. (B) Histological sections of BxPC3 xenograft stained with Prussian blue. The distribution of Resovist® and PEG–PAsp-coated magnetite nanoparticles, at 5.5 mg/kg with and without TGF-β inhibitor at 1 mg/kg, were examined 24 h after the administration. (C) Histological sections of liver stained with Prussian blue. The distribution of Resovist® and PEG–PAsp-coated magnetite nanoparticles, at 5.5 mg/kg with TGF-β inhibitor at 1 mg/kg, was examined 24 h after the administration. (D and E) Areas of iron staining in the tumor and liver were quantified. PEG–PAsp, PEG–PAsp coated magnetite nanoparticles with (+) and without (−) inhibitor. Error bars in the graphs represent standard errors of the mean ($n = 6$), and P values were calculated by two-tailed Student's t test. n.s.: not significant.

inhibitor with the i.v. administration of Resovist® or the PEG–PAsp-coated magnetite nanoparticles on their imaging capability in size-matched xenografts of the BxPC3 cell line. Fig. 6A shows the T_2-weighted MR images of the tumors at different time periods after the intravenous administration (preinjection, and 1 and 2 h postinjection) of PEG–PAsp-coated magnetite nanoparticles with and without TGF-β inhibitor.

Resovist® failed to image the tumor even with the co-administration of TGF-β inhibitor, presumably due to the non-specific accumulation into the reticuloendothelial system [8]. In contrast, the PEG–PAsp-coated magnetite nanoparticles exhibited significant negative enhancement of signal intensity in the tumor region of T_2-weighted images when combined with TGF-β inhibitor, suggesting the accumulation of detectable amounts of the PEG–PAsp-coated magnetite nanoparticles within 2 h after injection. Therefore, the difference in behavior of these two types of magnetite nanoparticles *in vivo* had a crucial importance in achieving effective tumor accumulation for successful MR imaging.

To further verify the accumulation of iron oxide nanoparticles in the tumor, we performed Prussian blue staining of the tumor tissues to detect iron oxide, which stains blue. As shown in Fig. 6B, positive staining of the tumor for iron oxide was only obvious in the condition with PEG–PAsp-coated nanoparticles combined with the TGF-β inhibitor. Areas of iron staining in the tumor were then quantified as seen in Fig. 6D, demonstrating a significant increase in the areas of positive staining by TGF-β inhibitor treatment. The presence of iron oxide was consistent with the MRI results. Iron oxide was observed in the area rich in fibrotic components, suggesting that the administration of TGF-β inhibitor transiently increases the permeability of the tumor capillary to promote the extravasation of the PEG–PAsp-coated magnetite nanoparticles, even though the BxPC3 tumor has the characteristic of hypovascularity [11].

Lastly, we examined liver tissues from the mice treated with Resovist® or the PEG–PAsp-coated magnetite nanoparticle, with or without TGF-β inhibitor, by iron staining (Fig. 6C). Although aggregates of Resovist® accumulated in the liver, particularly in cells with smaller nuclei (presumably Kuppfer cells), far less PEG–PAsp-coated magnetite nanoparticles accumulated in the liver without aggregation. These results did not differ with or without TGF-β inhibitor, which was determined by the area of Prussian blue staining (Fig. 6E).

4. Conclusion

In conclusion, we here demonstrated the physicochemical properties of PEG–PAsp-coated magnetite nanoparticles and the feasibility of these nanoparticles as MR contrast agents for cancer diagnosis. Improving the stability of nanoparticles might be important for enabling a longer half-life in the bloodstream and a better accumulation in tumor tissue, leading to effective MR imaging with contrast agents. The neutral ζ-potential of the PEG–PAsp-coated nanoparticle may contribute to avoidance of reticuloendothelial system uptake. Formation of the stable and dense PEG layer on the magnetite surface through the anchoring of PEG–PAsp by the monodentate chelation of COO^- residues to iron atoms definitely plays a substantial role in the increased stability of the nanoparticles *in vivo*. The use of PEG–PAsp-coated magnetite nanoparticles combined with a TGF-β inhibitor could thus become a novel regime in the diagnosis of intractable cancers, including pancreatic adenocarcinoma.

Acknowledgements

The authors thank Dr James R. Christie II, The University of Tokyo, for editing the English of the manuscript. This work was supported by a Grant-in-Aid for Scientific Research from the Ministry of Education, Culture, Sports, Science and Technology (MEXT), Core Research for Evolution of Science and Technology (CREST), Japan Science and Technology Corporation (JST), and the 21st century COE program 'Human-Friendly Materials based on Chemistry' from MEXT.

Appendix A. Supplementary data

Supplementary data associated with this article can be found, in the online version, at doi:10.1016/j.jconrel.2009.06.002.

References

[1] M.R. Dreher, W. Liu, C.R. Michelich, M.W. Dewhirst, F. Yuan, A. Chilkoti, Tumor vascular permeability, accumulation, and penetration of macromolecular drug carriers, J. Natl. Cancer Inst. 98 (5) (2006) 335–344.
[2] H.A. Burris, M.J. Moore, J. Andersen, M.R. Green, M.L. Rothenberg, M.R. Modiano, M.C. Cripps, R.K. Portenoy, A.M. Storniolo, P. Tarassoff, R. Nelson, F.A. Dorr, C.D. Stephens, D.D. Von Hoff, Improvements in survival and clinical benefit with gemcitabine as first-line therapy for patients with advanced pancreas cancer: a randomized trial, J. Clin. Oncol. 15 (6) (1997) 2403–2413.
[3] D.V. Sahani, Z.K. Shah, O.A. Catalano, G.W. Boland, W.R. Brugge, Radiology of pancreatic adenocarcinoma: current status of imaging, J. Gastroenterol. Hepatol. 23 (1) (2008) 23–33.
[4] D.L. Huber, Synthesis, properties, and applications of iron nanoparticles, Small 1 (5) (2005) 482–501.
[5] R. Weissleder, G. Elidonzo, J. Wittenberg, C.A. Rabito, H.H. Bengele, L. Josephson, Ultrasmall superparamagnetic iron oxide: characterization of a new class of contrast agents for MR imaging, Radiology 175 (2) (1990) 489–493.
[6] M. Lewin, N. Carlesso, C.H. Tung, X.W. Tang, D. Cory, D.T. Scadden, R. Weissleder, Tat peptide-derivatized magnetic nanoparticles allow *in vivo* tracking and recovery of progenitor cells, Nat. Biotechnol. 18 (4) (2000) 410–414.
[7] Y.W. Jun, J.H. Lee, J. Cheon, Chemical design of nanoparticle probes for high-performance magnetic resonance imaging, Angew. Chem. Int. Ed. 47 (28) (2008) 5122–5135.
[8] D.D. Stark, R. Weissleder, G. Elizondo, et al., Superparamagnetic iron oxide: clinical application as a contrast agent for MR imaging of the liver, Radiology 168 (2) (1988) 297–301.
[9] T. Neuberger, B. Schöpf, H. Hofmann, M. Hofmann, B. von Rechenberg, Superparamagnetic nanoparticles for biomedical applications: possibilities and limitations of a new drug delivery system, J. Magn. Mater. 293 (1) (2005) 483–496.
[10] M. Kumagai, Y. Imai, T. Nakamura, Y. Yamasaki, M. Sekino, S. Ueno, K. Hanaoka, K. Kikuchi, T. Nagano, E. Kaneko, K. Shimokado, K. Kataoka, Iron hydroxide nanoparticles coated with poly(ethylene glycol)–poly(aspartic acid) block copolymer as novel magnetic resonance contrast agents for *in vivo* cancer imaging, Colloids Surf. B: Biointerfaces 56 (1–2) (2007) 174–181.
[11] M.R. Kano, Y. Bae, C. Iwata, Y. Morishita, M. Yashiro, M. Oka, T. Fujii, A. Komuro, K. Kiyono, M. Kaminishi, K. Hirakawa, Y. Ouchi, N. Nishiyama, K. Kataoka, K. Miyazono, Improvement of cancer-targeting therapy, using nanocarriers for intractable solid tumors by inhibition of TGF-β signaling, Proc. Natl. Acad. Sci. U. S. A. 104 (9) (2007) 3460–3465.
[12] Y. Matsumura, H. Maeda, A new concept for macromolecular therapeutics in cancer-chemotherapy-mechanism of tumoritropic accumulation of proteins and the antitumor agent SMANCS, Cancer Res. 46 (12) (1986) 6387–6392.
[13] N. Nishiyama, M. Yokoyama, T. Aoyagi, T. Okano, Y. Sakurai, K. Kataoka, Preparation and characterization of self-assembled polymer-metal complex micelle from cis-dichlorodiammineplatinum(II) and poly(ethylene glycol)–poly(alpha,beta-aspartic acid) block copolymer in an aqueous medium, Langmuir 15 (2) (1999) 377–383.
[14] E. Fukushima, S.B.W. Roeder (Eds.), Experimental pulse NMR: a nuts and bolts approach, Addison-Wesley, Reading, Mass, 1981, pp. 28–35.
[15] A.J.S. MacFadzean, L.J. Davis, Iron-staining erythrocytic inclusions with especial reference to acquired haemolytic anaemia, Glasgow Med. J. 28 (1947) 237–279.
[16] S. Takae, Y. Akiyama, H. Otsuka, T. Nakamura, Y. Nagasaki, K. Kataoka, Ligand density effect on biorecognition by PEGylated gold nanoparticles: regulated interaction of RCA120 lectin with lactose installed to the distal end of tethered PEG strands on gold surface, Biomacromolecules 6 (2) (2005) 818–824.
[17] L. Cromières, V. Moulin, B. Fourest, E. Giffaut, Physico-chemical characterization of the colloidal hematite/water interface: experimentation and modeling, Colloids Surf., A. Physicochem. Eng. Asp. 202 (1) (2002) 101–115.
[18] L.J. Kirwan, P.D. Fawell, W. van Bronswijk, In situ FTIR-ATR examination of poly (acrylic acid) adsorbed onto hematite at low pH, Langmuir 19 (14) (2003) 5802–5807.
[19] Y.X.J. Wang, S.M. Hussain, G.P. Krestin, Superparamagnetic iron oxide contrast agents: physicochemical characteristics and applications in MR imaging, Eur. Radiol. 11 (11) (2001) 2319–2331.
[20] S.R. Wan, J.S. Huang, M. Guo, H. Zhang, Y. Cao, H. Yan, K. Liuet, Biocompatible superparamagnetic iron oxide nanoparticle dispersions stabilized with poly (ethylene glycol)oligo(aspartic acid) hybrids, J. Biomed. Mater. Res. A 80A (4) (2007) 946–954.
[21] C.W. Jung, Surface-properties of superparamagnetic iron-oxide MR contrast agents — ferumoxides, ferumoxtran, ferumoxsil, Magn. Reson. Imaging 13 (5) (1995) 675–691.

Enhanced Percolation and Gene Expression in Tumor Hypoxia by PEGylated Polyplex Micelles

Muri Han[1], Makoto Oba[2], Nobuhiro Nishiyama[3,4], Mitsunobu R Kano[4,5], Shinae Kizaka-Kondoh[6] and Kazunori Kataoka[1,3,4,7]

[1]Department of Materials Engineering, Graduate School of Engineering, The University of Tokyo, Tokyo, Japan; [2]Department of Clinical Vascular Regeneration, Graduate School of Medicine, The University of Tokyo, Tokyo, Japan; [3]Center for Disease Biology and Integrative Medicine, Graduate School of Medicine, The University of Tokyo, Tokyo, Japan; [4]Center for NanoBio Integration, The University of Tokyo, Tokyo, Japan; [5]Department of Molecular Pathology, Graduate School of Medicine, The University of Tokyo, Tokyo, Japan; [6]Department of Radiation Oncology and Image-Applied Therapy, Kyoto University, Graduate School of Medicine, Kyoto, Japan; [7]Core Research for Evolutional Science and Technology (CREST), Japan Science and Technology Agency (JST), Kawaguchi, Japan

In regard to gene vectors for cancer gene therapy, their percolation into the tumor tissue should be essential for successful outcome. Here, we studied the tumor penetrability of nonviral vectors (polyplexes) after incubation with the multicellular tumor spheroid (MCTS) models and intratumoral (i.t.) injection into subcutaneous tumors. As a result, polyethylene glycolated (PEGylated), core–shell type polyplexes (polyplex micelles) showed facilitated percolation and improved transfection inside the tumor tissue, whereas conventional polyplexes from cationic polymers exhibited limited percolation and localized transfection. Furthermore, the transfection of hypoxia-responsive plasmid demonstrated that polyplex micelles allowed the transfection to the hypoxic region of the tumor tissue in both *in vitro* and *in vivo* experiments. To the best of our knowledge, our results demonstrated for the first time that polyplex micelles might show improved tumor penetrability over cationic polyplexes, thereby achieving transfection into the inside of the tumor tissue.

Received 22 December 2008; accepted 24 April 2009; published online 26 May 2009. doi:10.1038/mt.2009.119

INTRODUCTION

Gene therapy is a promising method for the treatment of malignant tumors, and its success relies on the capabilities of gene vectors. In this regard, nonviral vectors composed of plasmid DNA (pDNA) and cationic polymers, so-called polyplexes have been attracting much attention due to several advantages such as no immunogenicity, safety, and easy large-scale preparation.[1–4] So far, considerable efforts have been devoted to improve the transfection efficiency of polyplexes as well as control the gene expression in the body.[5–8] However, in regard to gene vectors for cancer gene therapy, much attention should be paid on another important property: percolation into the tumor tissue. In general, solid tumors are known to possess heterogeneous structures composed of blood vessels, interstitial tissues, clusters of tumor cells with normoxic and hypoxic regions. Therefore, it might be difficult to deliver the therapeutic agents to tumor cells distant from the vasculature.[9–11] Furthermore, hypoxic region induced by the insufficient blood supply is known to be inherently less susceptible to therapeutic agents.[10] As such difficulty in treating hypoxic regions is often correlated with recurrence and malignant progression of solid tumors,[10] overcoming the limited drug access to hypoxic cells should be a critical issue in cancer therapy. Thus, the percolation of gene vectors in solid tumors should be of primary importance to achieve successful cancer gene therapy.

Recently, we have developed a highly transfectable but less-toxic core–shell type polyplex with poly(ethylene glycol) (PEG) palisades (polyplex micelle), which was formed through the electrostatic interaction between pDNA and PEG-*b*-polyaspartamide having 1,2-diaminoethane side chain (PEG-*b*-P[Asp(DET)]) (**Figure 1**).[12,13] This polyplex micelle showed remarkable features, including efficient gene transfer to primary cells,[12] successful *in vivo* transfection to a rabbit carotid artery,[14] and transfection-mediated bone regeneration.[15] In this study, we explored the tumor penetrability of polyplex micelles, because we have recently demonstrated that amphiphilic block copolymer micelles can show penetrability into multicellular tumor spheroids (MCTSs)[16] as well as solid tumors after intravenous administration.[17] Here, we demonstrated that polyplex micelles from PEG-*b*-P[Asp(DET)] showed successful transfection to hypoxic cells inside MCTS as well as enhanced percolation and widely distributed gene expression within the tumor tissue after intratumoral (i.t.) injection. In contrast, cationic polyplexes showed limited penetration and localized transfection in both *in vitro* and *in vivo* studies. These results suggest that polyplex micelles may overcome the transport barrier of nonviral vectors, facilitating their use for cancer gene therapy.

RESULTS

Transfection to MCTS

MCTS is an appropriate *in vitro* tumor model representing morphological and functional features of *in vivo* avascular solid tumors, and is composed of actively proliferating outer cell layers

Correspondence: Kazunori Kataoka, Department of Materials Engineering, Graduate School of Engineering, The University of Tokyo, 7-3-1 Hongo, Bunkyo-ku, Tokyo 113-8656, Japan. E-mail: kataoka@bmw.t.u-tokyo.ac.jp

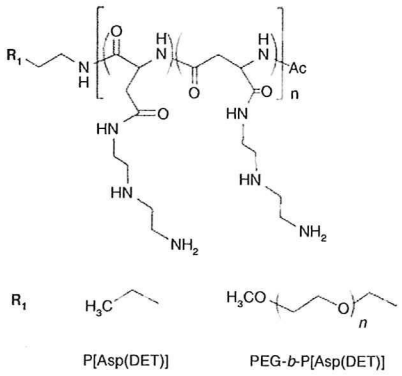

Figure 1 Chemical structures of P[Asp(DET)] homopolymers and PEG-*b*-P[Asp(DET)] block copolymers.

and hypoxic and quiescent inner cells.[18] In this study, a large-sized MCTS (400–500 μm), which possessed a hypoxic region characterized by necrotic cells inside due to limited supply of oxygen and nutrition (**Figure 2a**), was transfected with pCAcc + *Venus* by using the linear polyethylenimine (LPEI) and P[Asp(DET)] polyplexes and PEG-*b*-P[Asp(DET)] polyplex micelles at a defined mixing ratio of the number of amino groups units to a nucleotide unit (N/P ratio). Note that, although we have recently reported that a small-sized MCTS (~100 μm) can be disrupted by the cytotoxicity of polyplexes,[19] the large-sized MCTS used in this study is stable against the polyplex-mediated transfection. The expression of a variant of yellow fluorescent protein, *Venus* was evaluated by confocal microscopic observation. At 48 hours after the transfection (24-hour incubation and additional 24-hour incubation after the medium replacement), the LPEI polyplexes (N/P = 6, the manufacturer's recommendation ratio) and P[Asp(DET)] polyplexes (N/P = 20) showed significant gene expression limited to the periphery of the MCTS (**Figure 2b**). This result indicates that cationic polyplexes might lack the ability to transfect the inside of the MCTS. In contrast, PEG-*b*-P[Asp(DET)] polyplex micelles (N/P = 20) showed appreciable gene expression at not only the periphery but also the inside of the MCTS (**Figure 2b**), where a great number of necrotic cells were observed as indicated by red fluorescence from ethidium homodimer (EthD-1) (**Figure 2c**). These results suggest that polyplex micelles may allow the gene transfer to tumor cells in the hypoxic inner region of the MCTS.

Hypoxia-selective gene expression in the MCTS

To confirm the gene expression in hypoxic cells in the MCTS, we carried out the transfection study using pDNA encoding *Venus* driven by the 5× hypoxia-responsive element (5HRE) promoter (p5HRE + *Venus*). The hypoxia-selectivity of p5HRE + *Venus* was examined in monolayer cultured HuH-7 cells under hypoxic conditions reproduced by iron-chelating agent, deferoxamine mesylate.[20] As shown in **Figure 3a**, PEG-*b*-P[Asp(DET)] polyplex micelles containing hypoxia-responsive p5HRE + *Venus* showed no gene expression under normoxic conditions (0 μmol/l deferoxamine mesylate) but an appreciable gene expression under hypoxia-mimicking conditions (200 μmol/l deferoxamine mesylate). Note that polyplex micelles containing hypoxia-irresponsive pCAcc + *Venus* exhibited significant

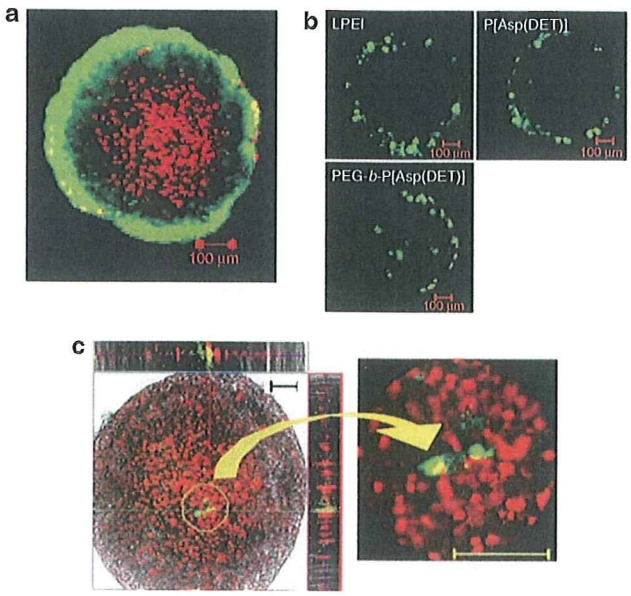

Figure 2 Transfection to HuH-7 MCTS. **(a)** Live/dead staining of HuH-7 spheroid (optical slice at the middle of spheroid. Bar = 100 μm). The green and red fluorescence are derived from live and dead cells, respectively. **(b)** Gene expression of pCAcc + *Venus* in HuH-7 MCTS transfected with LPEI polyplexes (N/P = 6), P[Asp(DET)] polyplexes (N/P = 20), and PEG-*b*-P[Asp(DET)] polyplex micelles (N/P = 20) (24 hours of incubation time and 24 hours of additional incubation after the medium replacement). **(c)** Gene expression of pCAcc + *Venus* at the inner region of HuH-7 MCTS transfected with PEG-*b*-P[Asp(DET)] polyplex micelles (N/P = 20) (24 hours of incubation time and 24 hours of additional incubation after the medium replacement) (Left: The red and green fluorescence are derived from dead cells and transfected protein *Venus*, respectively. Right: Magnified image of the circled region in the left picture). LPEI, linear polyethylenimine; MCTS, multicellular tumor spheroid; N/P, ratio of the number of amino groups units to a nucleotide unit.

gene expression under both normoxic and hypoxic conditions. Thus, p5HRE + *Venus* was demonstrated to be highly selective to hypoxic environments. Then, LPEI and P[Asp(DET)] polyplexes and PEG-*b*-P[Asp(DET)] polyplex micelles containing p5HRE + *Venus* were applied to the transfection to the large-sized MCTS (400–500 μm). As a result, none of 5 spheroids transfected with LPEI polyplexes showed the expression of p5HRE + *Venus* (data not shown), which may be consistent with the expression of pCAcc + *Venus* limited to the periphery of the MCTS (**Figure 2b**). Surprisingly, P[Asp(DET)] polyplexes exhibited the expression of p5HRE + *Venus* in two of five spheroids at 48 hours after the transfection; however, the gene expression was limited to the outer rims of hypoxic regions at ~100 μm distance from the periphery of the MCTS (**Figure 3b**; the yellow circle is the initial size of spheroids before the transfection). This result suggests that P[Asp(DET)] polyplexes could penetrate into the inside of the spheroids to some extent. In contrast, PEG-*b*-P[Asp(DET)] polyplex micelles allowed the transfection of p5HRE + *Venus* to a larger number of the cells in the inner region of the MCTS in 7 of 10 spheroids (**Figure 3b**), suggesting the ability of the polyplex micelles to transfect hypoxic cells inside of the spheroids. To further confirm this effect, two distinct plasmids encoding DsRedC1 (red fluorescence) driven

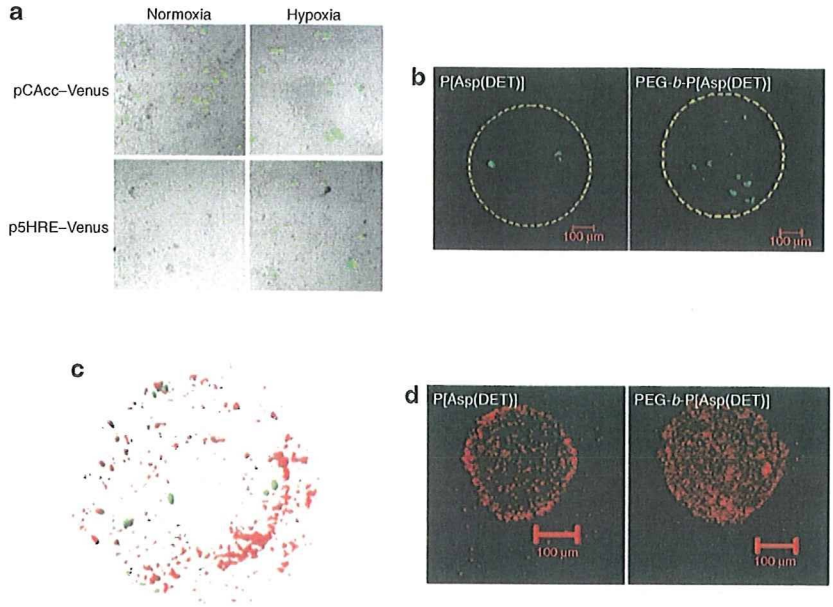

Figure 3 Hypoxia selective gene expression in the MCTS. **(a)** Gene expressions of hypoxia-irresponsive pCAcc + *Venus* and hypoxia-responsive p5HRE + *Venus* in monolayer cultured HuH-7 cells under normoxic and hypoxic conditions. HuH-7 cells were incubated with PEG-*b*-P[Asp(DET)] polyplex micelles (N/P = 20) for 24 hours, followed by additional 24 hours incubation after the medium replacement. Hypoxia-mimicking conditions were reproduced by incubating the cells with iron chelating agent, DFx during the postincubation. **(b)** Gene expressions of hypoxia-responsive p5HRE + *Venus* in the HuH-7 spheroids transfected with P[Asp(DET)] polyplexes and PEG-*b*-P[Asp(DET)] polyplex micelles (N/P = 20). The yellow circle indicates the size of the MCTS at the time of the transfection. **(c)** Piled up images of the gene expressions of hypoxia-irresponsive pCMV-DsRedC1 (red fluorescence) and hypoxia-responsive p5HRE – *Venus* (green fluorescence) in the MCTS transfected with PEG-*b*-P[Asp(DET)] polyplex micelles incorporating each plasmid (N/P = 20). **(d)** Distribution of Cy3-labeled pDNA encapsulated into P[Asp(DET)] polyplexes (N/P = 20) and PEG-*b*-P[Asp(DET)] polyplex micelles (N/P = 20) in HuH-7 MCTS after 24-hour incubation. The images were taken at the center of the spheroids. DFx, deferoxamine mesylate; MCTS, multicellular tumor spheroid; N/P, ratio of the number of amino groups units to a nucleotide unit.

by the cytomegalovirus (CMV) promoter (pCMV-DsRedC1) and *Venus* (green fluorescence) driven by the 5HRE promoter (p5HRE – *Venus*) were independently encapsulated into PEG-*b*-P[Asp(DET)] polyplex micelles, and then applied to the transfection to the MCTS. After 48 hours, optical slices of the MCTS at a depth of 1 μm were taken by confocal microscopy, and then piled up by Imaris software (Carl Zeiss, Jena, Germany) to obtain the three-dimensional localization of each fluorescence. As shown in **Figure 3c**, the expression of p5HRE – *Venus* was mainly detected in the inner region of the MCTS, whereas the expression of pCMV-DsRedC1 was observed throughout the MCTS. Thus, the hypoxic inner regions of the MCTS were successfully transfected with PEG-*b*-P[Asp(DET)] polyplex micelles.

Percolation of polyplexes and polyplex micelles into the MCTS

The percolation of the polyplexes and polyplex micelles into the MCTS was investigated by using Cy3-labeled pDNA. In this study, the MCTS with a diameter of 200–250 μm was used to detect weak fluorescence from Cy3-labeled pDNA within the spheroids. **Figure 3d** shows the fluorescent image of Cy3-labeled pDNA at the center of HuH-7 MCTS after 24-hour incubation with polyplexes or polyplex micelles. Note that the treatment of the relatively small-sized MCTS with LPEI polyplexes resulted in destruction of spheroid structures due to the cytotoxicity of LPEI as previously reported.[19] As shown in **Figure 3d**, P[Asp(DET)] polyplexes displayed apparent fluorescence at the periphery of spheroids. This result is consistent with the previous report that cationic polyplexes could penetrate only the outer 3–5 proliferating cell layers (10–20 μm) of the MCTS.[11] In contrast, the pDNA formulated in PEG-*b*-P[Asp(DET)] polyplex micelles showed well-distributed fluorescence within spheroids, suggesting their percolation into the inside of the spheroids. Similar results were obtained when the MCTS model from a different cell line (*i.e.*, human pancreatic BxPC3 cells) were used (**Supplementary Figure S1**). Thus, polyplex micelles might possess the ability to percolate into the spheroids over cationic polyplexes.

i.t. distribution of polyplexes and polyplex micelles after i.t. injection

The i.t. distribution of naked pDNA, LPEI polyplexes (N/P = 6), P[Asp(DET)] polyplexes (N/P = 20), or PEG-*b*-P[Asp(DET)] polyplex micelles (N/P = 20) after the injection to solid tumors (human pancreatic adenocarcinoma BxPC3 cells) was evaluated by using Cy3-labeled pDNA (n = 3). In this experiment, each formulation was coadministered with FluoSphere fluorescent microspheres [particle size: 15 μm, 645 nm/680 nm (Ex/Em)] as a marker for the injection point. The fluorescent images of Cy3-labeled pDNA in BxPC3 tumors are shown in **Figure 4a** and **Supplementary Figure S2**, and the total pixels of fluorescence area and its localization in the three different regions classified by the distance from the injection point (<100 μm, 100–200 μm, >200 μm) are quantified

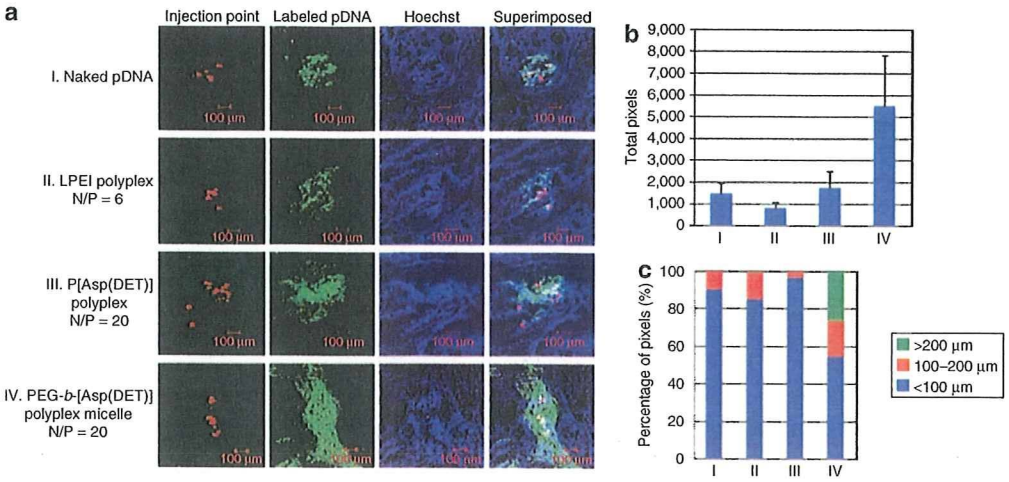

Figure 4 Intratumoral distribution of polyplexes and polyplex micelles after intratumoral injection. (**a**) Distribution of Cy3-labeled pDNA (green fluorescence) in a naked form or encapsulated into LPEI polyplexes (N/P = 6), P[Asp(DET)] polyplexes (N/P = 20), or PEG-*b*-P[Asp(DET)] polyplex micelles (N/P = 20) within human pancreatic adenocarcinoma BxPC3 tumors after intratumoral (i.t.) injection. The red and blue fluorescence are derived from fluorescent beads with a size of 15 μm as an indicator of injection point and Hoechst 33342 for the nuclear staining, respectively (more detailed data are shown in **Supplementary Figure S2**). (**b**) Total pixels and (**c**) percentage of pixels of fluorescent area of Cy3-labeled pDNA in three regions classified by the distance from the injection point. N/P, ratio of the number of amino groups units to a nucleotide unit.

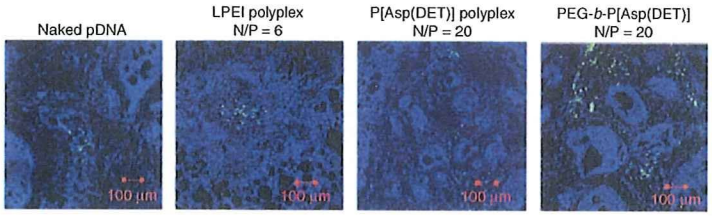

Figure 5 Gene expression of EGFP (green) within BxPC3 tumors at 6 days post-i.t. injection of naked plasmids, LPEI polyplexes (N/P = 6), P[Asp(DET)] polyplexes (N/P = 20), or PEG-b-P[Asp(DET)] polyplex micelles (N/P = 20). The blue fluorescence is derived from Hoechst 33342 for the nuclear staining. EGFP, enhanced green fluorescent protein; LPEI, linear polyethylenimine; N/P, ratio of the number of amino groups units to a nucleotide unit.

in Figure 4b,c, respectively. As a result, PEG-*b*-P[Asp(DET)] polyplex micelles showed a tendency to distribute more widely from the injection point compared with naked pDNA, LPEI and P[Asp(DET)] polyplexes. Note that irregular i.t. distribution of the polyplex micelles may be attributed to the heterogeneous structure of the BxPC3 tumors comprising clusters of dense tumor cells and interstitial tissues as indicated by the nuclear staining with Hoechst 33342.

In vivo gene expression after i.t. injection

The *in vivo* gene expression of fluorescent protein, enhanced green fluorescent protein (EGFP) within the BxPC3 tumors at 6 days post-i.t. injection of naked pDNA, LPEI polyplexes (N/P = 6), P[Asp(DET)] polyplexes (N/P = 20), or PEG-*b*-P[Asp(DET)] polyplex micelles (N/P = 20) was evaluated (n = 3). Note that P[Asp(DET)] polyplexes and polyplex micelles showed the highest transfection at 6 days postincubation in the MCTS models.[19] As shown in Figure 5, PEG-*b*-P[Asp(DET)] polyplex micelles apparently showed a widely distributed expression of EGFP in comparison with naked pDNA, LPEI, and P[Asp(DET)] polyplexes. These results seem to be consistent with the i.t. distribution of polyplex micelles (Figure 4).

Furthermore, the expression of hypoxia-responsive p5HRE + *Venus* within the BxPC3 tumors was evaluated (Figure 6a). The hypoxic region developed far from the vessels in the BxPC3 tumors was confirmed by fluorescein isothiocyanate-conjugated anti-Hypoxyprobe-1 monoclonal antibody (Figure 6b). Similar to Figure 4c, the pixels of fluorescent area in Figure 6a are classified into three different regions and summarized in Figure 6c. As a result, naked pDNA and LPEI polyplexes showed little gene expression, and P[Asp(DET)] polyplexes showed an appreciable gene expression in the region close to the injected point. In contrast, PEG-*b*-P[Asp(DET)] polyplex micelles showed well-distributed gene expression even in the furthest region from the injection point (>200 μm). These results suggest that the polyplex micelles might have the ability to percolate into the tumor tissue, thereby improving the gene transfection in the hypoxic regions of solid tumors.

DISCUSSION

Recently, we compared the transfection ability and cytotoxicity between P[Asp(DET)] polyplexes and PEG-*b*-P[Asp(DET)] polyplex micelles by using MCTS models.[19] We revealed that the PEGylation decreased the cytotoxicity of polyplexes without

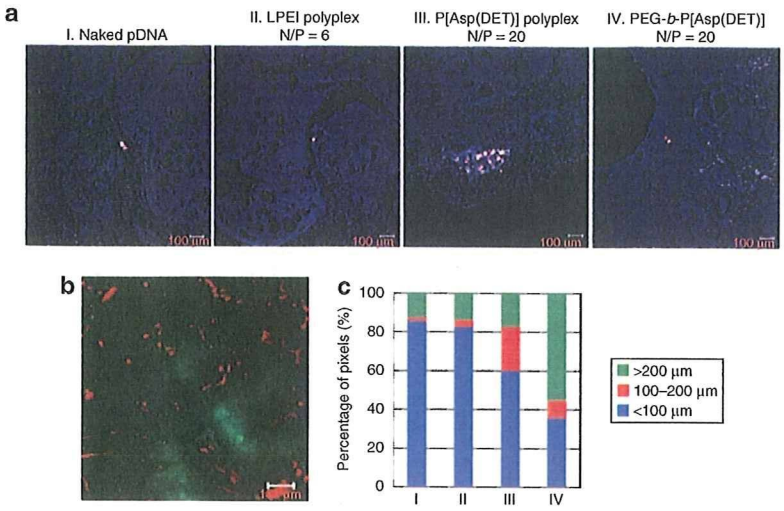

Figure 6 Hypoxia-responsive gene expression after intratumoral injection. **(a)** Gene expression of hypoxia-responsive p5HRE + *Venus* (white) within BxPC3 tumors at 6 days post-i.t. injection of naked plasmids, LPEI polyplexes (N/P = 6), P[Asp(DET)] polyplexes (N/P = 20), or PEG-b-P[Asp(DET)] polyplex micelles (N/P = 20). The red and blue fluorescence are derived from fluorescent beads with a size of 15 μm as an indicator of injection point and Hoechst 33342 for the nuclear staining, respectively. **(b)** Hypoxic regions in BxPC3 solid tumors. The red and green fluorescence are derived from anti-PECAM-1 antibody and anti-Hypoxyprobe-1 antibody, respectively. **(c)** Percentage of pixels of fluorescent area of transfected *Venus* protein in three regions classified by the distance from the injection point. i.t., intratumoral; LPEI, linear polyethylenimine; N/P, ratio of the number of amino groups units to a nucleotide unit.

compromising the transfection efficiency, while delaying the onset of gene expression. In this study, we report another important property of PEG-*b*-P[Asp(DET)] polyplex micelles, *i.e.*, tissue penetrability. We demonstrated that polyplex micelles showed facilitated percolation of loaded pDNA into the tumor tissue in both *in vitro* MCTS models and subcutaneous tumor models. Consequently, polyplex micelles showed a well-distributed gene expression after i.t. injection, allowing the transfection to the hypoxic regions of the tumors. These observations are in good agreement with our previous reports that polymeric micelles incorporating adriamycin showed enhanced percolation into the tumor tissue not only in the MCTS models[16] but also in subcutaneous tumors after intravenous administration.[17] Recently, Mellor *et al.* reported that cationic polyplexes from linear and branched PEI and lipoplexes showed penetration and transfection limited to the outer 3–5 proliferating cell layers in the large-sized MCTS (~474 nm).[11] Consistently, our results (**Figures 2b, 3d**, and **4–6**) also demonstrated not only *in vitro* but also *in vivo* that cationic polyplexes might show the limited penetration and localized transfection within the tumor. Furthermore, the result indicates for the first time that PEGylated polyplexes led loaded pDNA to show improved tissue penetrability compared with cationic polyplexes, exerting the appreciable gene expression in the inner hypoxia region.

PEGylation has apparently an advantage to prevent aggregation of polyplexes in the physiological condition with the presence of considerable amount of salt. Also, the PEGylation effectively masks the cationic nature of the core polyplexes, preventing nonspecific interaction serum proteins and extracellular matrices. Indeed, we observed that the PEG shielding of the P[Asp(DET)] polyplexes decreased the Zeta-potential from +30 mV to +6 mV. Such prevention of aggregate formation and reduced interaction with biological components by PEGylation may contribute to the facilitated percolation of the polyplexes into the tumor tissue. In this regard, the stability of polyplex micelles is an important issue during their penetration process into the tumor tissue. Our previous study revealed that the PEG-*b*-P[Asp(DET)] polyplex micelles showed much higher tolerability against the pDNA exchange reaction with an anionic lipid compared with the P[Asp(DET)] polyplexes.[19] Such increased stability of polyplex micelles is consistent with their improved penetration into the tumor tissue observed here. Furthermore, there are several reports that PEGylated nanoparticles show enhanced passage through the mucosal tissues to overcome intestinal barriers presumably due to the high flexibility and amphiphilicity of PEG chains.[21–23]

The detailed mechanisms of the enhanced percolation of polyplex micelles in the tumor tissue remain to be clarified yet; however, the results in this study clearly demonstrate that polyplex micelles might access the tumor cells in the hypoxic region with the intrinsic functions to deliver therapeutic genes. Thus, polyplex micelles are expected to treat hypoxic regions in the tumor tissue, potentially preventing the recurrence and malignant progression of solid tumors. Together with improved pharmacokinetic parameters, PEGylated polyplexes with a high tissue-percolation property might be promising nonviral vectors for *in vivo* cancer gene therapy.

MATERIALS AND METHODS

Plasmid DNA. The plasmid, pCAcc vector having CAG promoter,[24] was provided by RIKEN Bioresource Center (Ibaraki, Japan). Also, a fragment cDNA of SEYFP-F46L (*Venus*), which is a variant of yellow fluorescent protein with the mutation F46L,[25] was provided by A. Miyawaki at the Brain Science Institute, RIKEN and inserted into the pCAcc vector (pCAcc + *Venus*). Each pDNA was amplified in competent DH5α *Escherichia coli* and purified using HiSpeed Plasmid MaxiKit (Qiagen Sciences, Hilden, Germany). The plasmid, pGL5 vector having p5HRE, was provided by Faculty of Medicine, Kyoto University (Japan).[26] The DNA fragment encoding *Venus* was inserted between *Hind*III and *Xba*I sites of pGL3/5xHRE/CMVmp.

Nonviral vectors. LPEI (ExGen 500, 22 kd) was purchased from Fermentas (Burlington, Ontario, Canada). P[Asp(DET)] and PEG-*b*-P[Asp(DET)] were prepared as previously reported.[12–14] Briefly, β-benzyl-L-aspartate *N*-carboxyanhydride was polymerized by the initiation from the primary amino group of *n*-butylamine and MeO-PEG-NH_2 (M_w: 12,000) to obtain poly(β-benzyl L-aspartate) (PBLA) and PEG-*b*-PBLA, respectively. The degree of polymerization of PBLA was determined to be 98 for PBLA and 101 for PEG-*b*-PBLA by the ^1H NMR measurement. Then, PBLA and PEG-*b*-PBLA were reacted with diethylenetriamine (DET) (50 equiv to benzyl group of PBLA segment) under mild anhydrous conditions to obtain P[Asp(DET)] and PEG-*b*-P[Asp(DET)], respectively. The unimodal distribution and the almost 100% conversion of the BLA unit into Asp(DET) unit were confirmed by gel permeation chromatography and ^1H NMR measurements.

Preparation of polyplexes. Each polymer was mixed with pDNA in 10 mmol/l Tris–HCl (pH 7.4) at varying N/P ratios (final pDNA concentration: 100 μg/ml). Polyplex was applied to each well for transfection 30 minutes after preparation. Polyplex micelle was applied to each well for transfection after overnight incubation at ambient temperature.

Cell culture and preparation of MCTS. Human hepatoma HuH-7 cells (from JCRB Cell Bank, Osaka, Japan) and human pancreatic adenocarcinoma BxPC3 cells (from ATCC, Manassas, VA) were maintained in Dulbecco's modified Eagle's medium and RPMI 1640 medium, respectively, supplemented with 10% fetal bovine serum in a humidified atmosphere containing 5% CO_2 at 37 °C. MCTS were prepared by using the plate designed for spheroid formation (Sumiloncelltight; Sumitomo Bakelite, Tokyo, Japan) as reported previously.[15,18] The size of MCTS can be controlled by the incubation period. During the incubation, the medium was replaced by fresh medium containing 10% fetal bovine serum every 3 days.

Live/dead assay. Live and dead assay was accomplished with the Live/Dead kit protocol (Molecular Probes, Carlsbad, CA). MCTS was rinsed with PBS(−) and then incubated with a solution containing 0.8 μmol/l calcein AM [495 nm/515 nm (Ex/Em)] and 4 μmol/l EthD-1 (495 nm/635 nm) in PBS(−) for 3 hours at 37 °C, followed by the observation by LSM 510 confocal laser scanning microscope (CLSM) (Carl Zeiss).

Transfection to MCTS. MCTS was incubated for 6–8 days until the diameter became >400–500 μm. Then, each polyplex solution containing 1 μg pDNA was applied to each well for the transfection. After 24-hour incubation, the medium was replaced by fresh medium, followed by additional 24-hour incubation. The gene expression of the *Venus* or EGFP was then evaluated through the observation by CLSM.

Percolation of nonviral vectors into the MCTS. To visualize the distribution of nonviral vectors in MCTS, pDNA was labeled with Label IT Cy3 Labeling Kit (Mirus, Piscataway, NJ). In this experiment, MCTS with the diameter of 200–250 μm was incubated with polyplexes or polyplex micelles containing 1 μg Cy3-labeled pDNA for 24 hours. After 24-hour incubation, MCTS was harvested and rinsed, followed by observation by CLSM.

Animal models. BALB/c nude mice (female, 5 weeks old) were obtained from Charles River Laboratories (Tokyo, Japan). BxPC3 cells (5×10^6 cells in 100 μl of PBS) were injected subcutaneously into the BALB/c nude mice and allowed to grow for 2–3 weeks to reach the proliferative phase. All animal experimental protocols were performed in accordance with the policies of the Animal Ethics Committee of the University of Tokyo.

Percolation of nonviral vectors in solid tumors. After the tumor size reached 6–8 mm in a diameter, the mice received the i.t. injection of 2 μg Cy3-labeled pDNA in a naked or polyplex-encapsulated form [20 μl in 10 mmol/l HEPES buffer (pH 7.4)] by using the Hamilton Microliter Syringe (Hamilton, Reno, NV). In this experiment, 5 μl of FluoSpheres fluorescent microspheres (particle size: 15 μm, 645 nm/680 nm) were mixed with Cy3-labeled pDNA solution and simultaneously injected into the BxPC3 tumor for indication of the injection point. After 24 hours, the tumors were excised and fixed with 10% formalin and sucrose PBS(−), followed by freezing in dry-iced acetone. Frozen samples were sectioned at 10-μm thickness in a cryostat, and stained with Hoechst 33342 (Dojindo Laboratories, Tokyo, Japan). The fluorescent images were then observed by CLSM.

Transfection to solid tumors. According to the protocols for the percolation study, the tumor-bearing mice received the i.t. injection of 2 μg pCAcc + EGFP or p5HRE + *Venus* in a naked or polyplex-encapsulated form. The animals administered with pCAcc + EGFP were killed at 6 days postinjection, and the excised tumors were fixed as previously described. The fluorescence of frozen section of solid tumors was observed by CLSM. On the other hand, the animals administered with p5HRE + *Venus* were administered with Hypoxyprobe-1 (Millipore Chemicon, Billerica, MA) at 60 mg/kg via tail vein at 6 days postinjection, and then killed for removal of solid tumors. Frozen sections of the xenograft were stained with rat anti-PECAM-1 antibody (BD Pharmingen, Franklin Lakes, NJ), and subsequently stained with Alexa 594-conjugated anti-rat IgG antibody (Invitrogen Molecular Probes, Carlsbad, CA) and fluorescein isothiocyanate-conjugated anti-Hypoxyprobe-1 MAb. The section was further counter-stained with TOTO-3 (Invitrogen Molecular Probes), and the fluorescence images were captured by CLSM.

Quantitative analysis of fluorescent images. The pixels of fluorescent area of Cy3-labeled pDNA or transfected *Venus* protein in the tumor section were quantified by using the Image J software (http://rsb.info.nih.gov/ij/), and classified into three different regions by the distance from the injection point (<100 μm, 100–200 μm, >200 μm).

SUPPLEMENTARY MATERIAL

Figure S1. Distribution of labeled pDNA in BxPC3 MCTS transfected by each polyplex or polyplex micelles in intersectional profiles at the shown slices (Optical slice at the center of MCTS. Red fluorescence is Cy3 labeled-pDNA).

Figure S2. Distribution of Cy3-labeled pDNA (green fluorescence) in a naked form or encapsulated into LPEI polyplexes (N/P=6), P[Asp(DET)] polyplexes (N/P=20) or PEG-*b*-P[Asp(DET)] polyplex micelles (N/P=20) within human pancreatic adenocarcinoma BxPC3 tumors after the intratumoral injection.

ACKNOWLEDGMENTS

We thank Kotoe Date (the University of Tokyo) for technical assistance. This work was supported in part by the Core Research Program for Evolutional Science and Technology from Japan Science and Technology Agency.

REFERENCES

1. Boussif, O, Lezoualc'h, F, Zanta, MA, Mergny, MD, Scherman, D, Demeneix, B *et al.* (1995). A versatile vector for gene and oligonucleotide transfer into cells in culture and *in vivo*: polyethylenimine. *Proc Natl Acad Sci USA* **92**: 7297–7301.
2. Ogris, M and Wagner, E (2002). Targeting tumors with non-viral gene delivery systems. *Drug Discov Today* **7**: 479–485.
3. Merdan, T, Kopecek, J and Kissel, T (2002). Prospects for cationic polymers in gene and oligonucleotide therapy against cancer. *Adv Drug Deliv Rev* **54**: 715–758.
4. Pack, DW, Hoffman, AS, Pun, S and Stayton, PS (2005). Design and development of polymers for gene delivery. *Nat Rev Drug Discov* **4**: 581–593.
5. Erbacher, P, Roche, AC, Monsigny, M and Midoux, P (1995). Glycosylated polylysine/DNA complexes: gene transfer efficiency in relation with the size and the sugar substitution level of glycosylated polylysines and with the plasmid size. *Bioconjug Chem* **6**: 401–410.
6. Merdan, T, Callahan, J, Petersen, H, Kunath, K, Bakowsky, U, Kopecková, P *et al.* (2003). Pegylated polyethylenimine-Fab' antibody fragment conjugates for targeted gene delivery to human ovarian carcinoma cells. *Bioconjug Chem* **14**: 989–996.
7. Ogris, M, Brunner, S, Schüller, S, Kircheis, R and Wagner, E (1999). PEGylated DNA/transferrin-PEI complexes: reduced interaction with blood components, extended circulation in blood and potential for systemic gene delivery. *Gene Ther* **6**: 595–605.

8. Harada-Shiba, M, Yamauchi, K, Harada, A, Takamisawa, I, Shimokado, K and Kataoka, K (2002). Polyion complex micelles as vectors in gene therapy—pharmacokinetics and *in vivo* gene transfer. *Gene Ther* **9**: 407–414.
9. Jain, RK (2001). Delivery of molecular and cellular medicine to solid tumors. *Adv Drug Deliv Rev* **46**: 149–168.
10. Minchinton, AI and Tannock, IF (2006). Drug penetration in solid tumours. *Nat Rev Cancer* **6**: 583–592.
11. Mellor, HR, Davies, LA, Caspar, H, Pringle, CR, Hyde, SC, Gill, DR *et al.* (2006). Optimising non-viral gene delivery in a tumour spheroid model. *J Gene Med* **8**: 1160–1170.
12. Kanayama, N, Fukushima, S, Nishiyama, N, Itaka, K, Jang, WD, Miyata, K *et al.* (2006). A PEG-based biocompatible block catiomer with high buffering capacity for the construction of polyplex micelles showing efficient gene transfer toward primary cells. *ChemMedChem* **1**: 439–444.
13. Miyata, K, Oba, M, Nakanishi, M, Fukushima, S, Yamasaki, Y, Koyama, H *et al.* (2008). Polyplexes from poly(aspartamide) bearing 1,2-diaminoethane side chains induce pH-selective, endosomal membrane destabilization with amplified transfection and negligible cytotoxicity. *J Am Chem Soc* **130**: 16287–16294.
14. Akagi, D, Oba, M, Koyama, H, Nishiyama, N, Fukushima, S, Miyata, T *et al.* (2007). Biocompatible micellar nanovectors achieve efficient gene transfer to vascular lesions without cytotoxicity and thrombus formation. *Gene Ther* **14**: 1029–1038.
15. Itaka, K, Ohba, S, Miyata, K, Kawaguchi, H, Nakamura, K, Takato, T *et al.* (2007). Bone regeneration by regulated *in vivo* gene transfer using biocompatible polyplex nanomicelles. *Mol Ther* **15**: 1655–1662.
16. Bae, Y, Nishiyama, N, Fukushima, S, Koyama, H, Yasuhiro, M and Kataoka, K (2005). Preparation and biological characterization of polymeric micelle drug carriers with intracellular pH-triggered drug release property: tumor permeability, controlled subcellular drug distribution, and enhanced *in vivo* antitumor efficacy. *Bioconjug Chem* **16**: 122–130.
17. Kano, MR, Bae, Y, Iwata, C, Morishita, Y, Yashiro, M, Oka, M *et al.* (2007). Improvement of cancer-targeting therapy, using nanocarriers for intractable solid tumors by inhibition of TGF-beta signaling. *Proc Natl Acad Sci USA* **104**: 3460–3465.
18. Sutherland, RM (1988). Cell and environment interactions in tumor microregions: the multicell spheroid model. *Science* **240**: 177–184.
19. Han, M, Bae, Y, Nishiyama, N, Miyata, K, Oba, M and Kataoka, K (2007). Transfection study using multicellular tumor spheroids for screening non-viral polymeric gene vectors with low cytotoxicity and high transfection efficiencies. *J Control Release* **121**: 38–48.
20. An, WG, Kanekal, M, Simon, MC, Maltepe, E, Blagosklonny, MV and Neckers, LM (1998). Stabilization of wild-type p53 by hypoxia-inducible factor 1alpha. *Nature* **392**: 405–408.
21. Huang, Y, Leobandung, W, Foss, A and Peppas, NA (2000). Molecular aspects of muco- and bioadhesion: tethered structures and site-specific surfaces. *J Control Release* **65**: 63–71.
22. Samuel, KL, Elizabeth, OD, Harrold, S, Man, ST, Wang, Y, Cone, R *et al.* (2007). Rapid transport of large polymeric nanoparticles in fresh undiluted human mucus. *Proc Natl Acad Sci USA* **104**: 1482–1487.
23. Yoncheva, K, Guembe, L, Campanero, MA and Irache, JM (2007). Evaluation of bioadhesive potential and intestinal transport of pegylated poly(anhydride) nanoparticles. *Int J Pharm* **334**: 156–165.
24. Niwa, H, Yamamura, K and Miyazaki, J (1991). Efficient selection for high-expression transfectants with a novel eukaryotic vector. *Gene* **108**: 193–199.
25. Nagai, T, Ibata, K, Park, ES, Kubota, M, Mikoshiba, K and Miyawaki, A (2002). A variant of yellow fluorescent protein with fast and efficient maturation for cell-biological applications. *Nat Biotechnol* **20**: 87–90.
26. Harada, H, Kizaka-Kondoh, S and Hiraoka, M (2005). Optical imaging of tumor hypoxia and evaluation of efficacy of a hypoxia-targeting drug in living animals. *Mol Imaging* **4**: 182–193.

Advanced Drug Delivery Reviews 61 (2009) 327–338

Contents lists available at ScienceDirect

Advanced Drug Delivery Reviews

journal homepage: www.elsevier.com/locate/addr

Design and development of dendrimer photosensitizer-incorporated polymeric micelles for enhanced photodynamic therapy ☆

Nobuhiro Nishiyama [a,c], Yuji Morimoto [d], Woo-Dong Jang [e], Kazunori Kataoka [a,b,c,*]

[a] Center for Disease Biology and Integrative Medicine, Graduate School of Medicine, the University of Tokyo, Tokyo, Japan
[b] Department of Materials Engineering, Graduate School of Engineering, the University of Tokyo, Tokyo, Japan
[c] Center for Nano-Bio Integration, the University of Tokyo, Tokyo, Japan
[d] Department of Integrative Physiology and Bio-Nano Medicine, National Defense Medical College, Saitama, Japan
[e] Department of Chemistry, College of Science, Yonsei University, Seoul, Republic of Korea

ARTICLE INFO

Article history:
Received 13 November 2008
Accepted 26 January 2009
Available online 4 February 2009

Keywords:
Photodynamic therapy (PDT)
Photosensitizers (PSs)
Dendrimers
Polymeric micelles
Photodynamic diagnosis (PDD)
Photochemical internalization (PCI)

ABSTRACT

Photodynamic therapy (PDT), which involves systemic administration of photosensitizers (PSs) followed by local photoillumination, is a promising method for the treatment of solid tumors and other diseases. Recently, considerable efforts have been devoted to the development of nanocarriers for the PS delivery with the aim of avoiding non-specific phototoxicity to normal tissues such as the skin. Here, we discuss the biological significance of the use of nanocarrier-encapsulated PSs in PDT. Also, we report our recent achievements on the development of dendrimer photosensitizer-loaded micelles as nanocarriers for PS delivery. We found that our nanocarriers greatly enhanced the PDT efficacy in vitro and in vivo, and also significantly reduced the skin phototoxicity. These results indicate the importance of a development strategy for nanocarriers and their great potential for clinical use. In addition, this review discusses the development of nanocarriers for emerging PDT-related technologies such as photodynamic diagnosis (PDD) and photochemical internalization (PCI).

Contents

1. Introduction . . . 327
2. Photodynamic therapy (PDT) with nanocarrier-encapsulated photosensitizers (PSs) . . . 328
 2.1. Biodistribution of nanocarrier-encapsulated PSs . . . 328
 2.2. In vivo mechanisms of PDT . . . 329
3. Polymeric micelles encapsulating dendrimer photosensitizers for enhanced PDT . . . 330
 3.1. Development of dendrimer photosensitizer-loaded micelles . . . 330
 3.2. In vitro PDT effect of dendrimer photosensitizer-loaded micelles . . . 331
 3.3. In vivo PDT effect of dendrimer photosensitizer-loaded micelles . . . 333
4. Photodymamic diagnosis (PDD)-guided PDT . . . 333
5. Development of light-sensitive nanocarriers utilizing photochemical internalization (PCI) . . . 334
6. Conclusion . . . 336
Acknowledgments . . . 336
References . . . 336

1. Introduction

Photodynamic therapy (PDT) is a promising method for the localized treatment of several diseases, including solid tumors [1–3]. PDT involves the systemic administration of photosensitizers (PSs) such as porphyrin and phthalocyanine derivatives, followed by photoactivation of PSs at the disease site with light of a specific wavelength. As illustrated in Fig. 1, PSs in a singlet state at the lowest or ground

☆ This review is part of the *Advanced Drug Delivery Reviews* theme issue on "Controlling Oxidative Stress: Therapeutic and Delivery Strategies".

* Corresponding author. Department of Materials Engineering, Graduate School of Engineering, The University of Tokyo, 7-3-1 Hongo, Bunkyo-ku, Tokyo 113-8656, Japan. Tel.: +81 3 5841 7138; fax: +81 3 5841 7139.
E-mail address: kataoka@bmw.t.u-tokyo.ac.jp (K. Kataoka).

0169-409X/$ – see front matter © 2009 Elsevier B.V. All rights reserved.
doi:10.1016/j.addr.2009.01.004

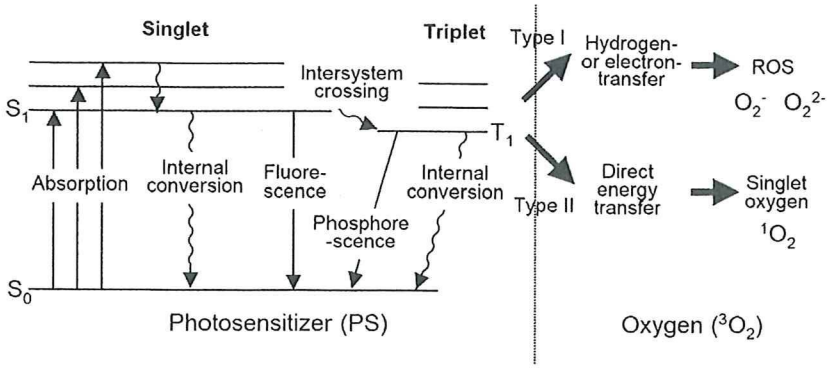

Fig. 1. Jablonski diagram showing the energy transfer from photosensitizers (PSs) to molecular oxygen.

state energy level (S_0) absorb a photon of the light of a specific wavelength to enter an excited state (S_1). PSs in the short-lived excited state return to the ground state by emitting fluorescence or by internal conversion with energy loss as heat, and also can be converted to the excited triplet state (T_1) with a longer lifetime via an intersystem crossing process. PSs in the triplet state return to the ground state by emitting phosphorescence, and also can transfer energy to other molecules by type I and type II reaction processes. In the type I reaction, free radicals formed by the hydrogen- or electron-transfer from PSs react with oxygen, thereby producing reactive oxygen species, including superoxide (O_2^-) and peroxide anions (O_2^{2-}). In the type II reaction, PSs in the excited triplet state directly transfer energy to molecular oxygen in a triplet ground state ($^3O_2$), resulting in the formation of highly reactive singlet oxygen ($^1O_2$). In PDT, these reactive oxygen species (ROS) oxidize (photodamage) subcellular organelles and other biomolecules, leading to light-induced cell death.

PDT has been shown to be effective against early-stage superficial cancers [1–4]. Also, PDT is non-invasive and has little or no effect on organ functions, so that it is recognized as a useful initial treatment for malignant tumors. Indeed, PDT using porfimer sodium (Photofrin®) has been approved for the treatment of oesophageal cancer in the United States and Canada, early- and late-stage lung cancer in the Netherlands, bladder cancer in Canada, and early-stage lung, oesophageal, gastric and cervical cancers in Japan [4]. However, PDT is often accompanied by long-lasting skin toxicity, which is a major limitation in the clinical application [1–4]. This is mainly due to the unfavorable biodistribution of PSs [5]. Therefore, a challenge in PDT is to create tumor-specific PSs. In this regard, the use of nanocarriers is a promising method for the tumor-specific delivery of PSs. To date, a variety of nanocarriers, including polymer-PS conjugates [6,7], long-circulating liposomes [8] and polymeric micelles [9–24], have been developed, because they have been demonstrated to show tumor-selective accumulation due to the enhanced microvascular permeability and impaired lymphatic drainage in the tumor tissue, a phenomenon which Maeda et al. termed the enhanced permeability and retention (EPR) effect [25–28]. Recently, we also developed a new PS formulation based on polymeric micelles encapsulating dendrimer photosensitizers, and demonstrated its remarkable efficacy in vitro and in vivo [17–24,29]. This review deals with general concepts and considerations of PDT with nanocarrier-encapsulated PSs, and our recent progress in research on polymeric micelles encapsulating dendrimer photosensitizers.

2. Photodynamic therapy (PDT) with nanocarrier-encapsulated photosensitizers (PSs)

2.1. Biodistribution of nanocarrier-encapsulated PSs

In general, most PSs intravenously administered are rapidly cleared from the circulation, although some of the molecules bind to serum proteins such as albumin and low-density lipoprotein (LDL) and remain in circulation for a longer period [3]. PSs show some specificity to the tumor cells. This may be partially due to the facilitated uptake of LDL-bound PSs by tumor cells expressing a large number of LDL receptors on their surface [3,30,31]. However, such LDL-bound PSs can also be taken up by macrophages; therefore, localization of macrophages containing LDL-bound PSs in the skin may be responsible for the skin hyperphotosensitivity [3,30,31]. To circumvent such a side effect, considerable efforts have been devoted to the development of new PSs that accumulate quickly in the tumor tissue and show rapid clearance from the body. For example, taporfin sodium (Talaporfin), a second generation PS, shows rapid clearance from the skin and has been approved for the treatment of early-stage lung cancers in Japan [32,33]. Thus, PDT with Talaporfin can reduce the skin phototoxicity; however, the patient still needs to stay in a darkened room for at least 2 weeks.

The use of long-circulating nanocarriers for PS delivery seems to be contradictory to the aforementioned recent trends in the development of new PSs. Nevertheless, long-circulating nanocarriers preferentially accumulate in the tumor tissue due to the EPR effect. It is known that long-circulating nanocarriers can achieve a tumor/normal tissue (muscle) accumulation ratio higher than 10 [34], whereas most conventional PSs including chlorin e_6 and Photofrin have been reported to exhibit a value of less than 2 for this ratio [5]. Buchholz et al. reported that free meta-tetrahydroxyphenylchlorin (m-THPC) and a stealth liposomal formulation of m-THPC showed tumor/skin accumulation ratios of 1.55 ± 0.88 and 6.50 ± 3.18, respectively [35]. Thus, the nanocarrier-mediated PS delivery can achieve a higher tumor/skin ratio compared with administration of PS alone. In general, low molecular weight PSs are assumed to penetrate the endothelium by passive diffusion and eventually accumulate in various organs and tissues to some extent. Such non-specific PS accumulation in the skin and normal tissues seems to be inevitable, even if PSs show rapid clearance. In contrast, nanocarriers might not pass through the tight junctions of the vasculature in the tissues (with the exception of the liver, spleen, and tumor tissues, which possess leaky vasculatures), which could account for their ability to achieve reduced PS accumulation in the skin and normal tissues. Although the underlying mechanisms of this effect remain to be clarified, the high tumor-specificity of nanocarrier-encapsulated PSs ensures the effectiveness and safety of PDT.

At the same time, the prolonged retention of nanocarrier-encapsulated PSs in the tumor tissue enables PDT with multiple irradiations. Kopecek et al. demonstrated that, in the PDT with *N*-(2-hydroxypropyl) methacrylamide copolymer-mesochlorin e_6 conjugates (PHPMA-Me_6), multiple irradiation can achieve a higher antitumor effect than single irradiation with an equivalent light dose [6]. Since the PDT effect depends on the oxygen concentration in the tumor tissue, a single excessive photoirradiation may consume considerable amounts of

oxygen, resulting in limited therapeutic efficacy. In contrast, double irradiation with a time lag allows oxygen to be reaccumulated in the tumor tissue, enhancing the efficacy of PDT.

2.2. In vivo mechanisms of PDT

The in vivo mechanisms of the anti-tumor effect of PDT are rather complicated. As illustrated in Fig. 2, several different but mutually related effects are involved. First, ROS generated from PSs can directly kill tumor cells. Second, PDT can damage the tumor vasculature, leading to vascular collapse and embolization [1]. And finally, PDT can activate anti-tumor immunity [40].

In regard to the first mechanism, the killing of tumor cells by ROS, it is difficult to achieve complete tumor eradication by this mechanism alone due to the generally non-uniform distribution of PSs in the tumor tissue. Such uneven distribution may be due to at least two causes: the difficulty of delivering therapeutic agents to tumor cells distant from the vasculature [36,37], and the restriction of drug penetration into solid tumors by increased interstitial fluid pressure (IFP) in the tumor tissue [37]. Both these problems may also be relevant to PDT using nanocarriers. To address them, we have recently explored the tumor-penetrability of polymeric micelles and found that polymeric micelles incorporating doxorubicin (Dox) showed penetrability into multicellular tumor spheroids [38] as well as solid tumors after intravenous administration [39]. These results were in contrast to those for the intratumoral distribution of Doxil®, a stealth liposomal formulation of Dox, which showed localized accumulation in perivascular regions and stromal tissues [39], although the underlying mechanisms remain to be clarified. Thus, there is a possibility that the use of polymeric micelles may overcome the limitations in the penetration into solid tumors. In addition to a non-uniform intratumoral distribution of PSs, limited oxygen supply due to the above-mentioned features of solid tumors as well as oxygen consumption during PDT might also decrease the PDT efficacy. This can be partially solved by multiple light irradiation. In this regard, nanocarriers might have a great advantage due to their prolonged retention property in solid tumors as described in Section 2.1.

In the second mechanism, PDT-induced vascular collapse and embolization abolishes the supply of oxygen and nutrients to the tumor cells, resulting in tumor destruction. We previously reported that the vessels treated with PDT using dendrimer porphyrin (DP)-loaded micelles regressed to collagen tubes without endothelial cells or were occluded by erythrocytes [21]. Such vascular collapse and embolization by PDT may also affect the accumulation of nanocarriers in the tumor tissue—i.e., this effect may shut out the outward convective flow by elevated IFP in the tumor tissue and improve the retention of nanocarriers in the tumor tissue. In this regard, Kopecek et al. reported that combination therapy using PDT with PHPMA-Me_6 and chemotherapy with PHPMA-Dox conjugates was much more effective than the multiple chemotherapy with PHPMA-Dox [6]. It is possible that the vascular damage by PDT may improve the retention of PHPMA-Dox in the tumor tissue.

As stated above, the third mechanism involves the activation of anti-tumor immunity by PDT [40]. This is unusual in that most cancer therapies—including surgical resection and chemotherapy—are immunosuppressive, whereas PDT is immunostimulatory. PDT induces acute inflammation through the release of proinflammatory cytokines such as tumor necrosis factor-α (TNF-α) and interleukin (IL)-1 and IL-6, and thereby attracts leukocytes such as dendritic cells (DCs) and neutrophils. On the other hand, PDT induces necrosis or apoptosis of tumor cells, thereby stimulating the production of tumor cell-derived antigens. Such alterations of the tumor microenvironment by PDT might increase the antigen cross-presentation efficiency of DCs and facilitate their maturation, leading to induction of $CD8^+$ cytotoxic T cells. Therefore, PDT can cause not only local destruction of primary tumors but also a systemic antitumor effect when used in combination with immunostimulatory therapies, ultimately leading to complete eradication of malignant tumors without recurrence and metastasis [41,42]. For example, Engleman et al. reported that local PDT followed by intratumoral injection of naive DCs induced systemic antitumor immunity that inhibited the growth of untreated tumors at the distant site, including multiple lung metastases. These effects were mediated mainly by $CD8^+$ cytotoxic T cells [41].

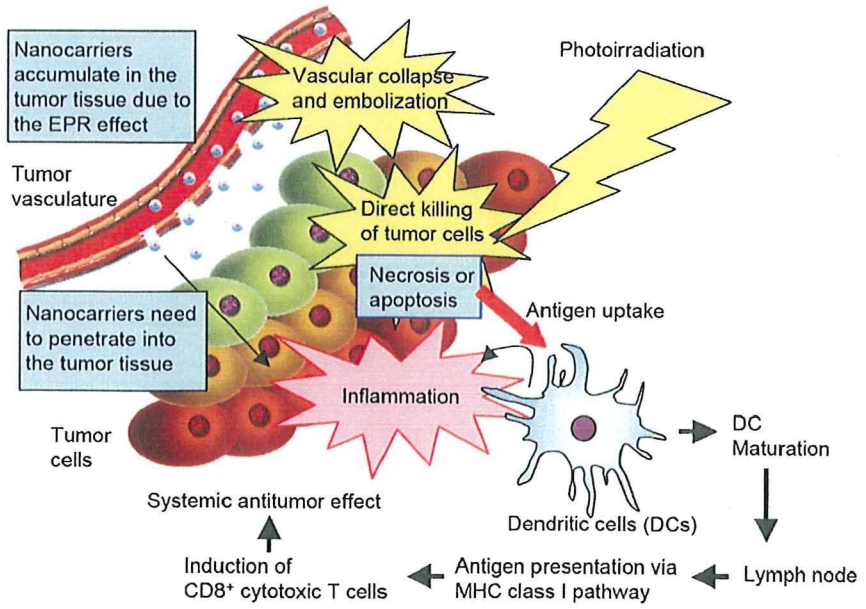

Fig. 2. In vivo mechanisms of PDT. The nanocarrier-encapsulated PSs accumulate in the tumor tissue by the enhanced permeability and retention (EPR) effect. Upon photoirradiation, reactive oxygen species (ROS) generated from PSs can directly kill tumor cells. PDT can also cause vascular collapse and embolization, leading to tumor destruction through a lack of oxygen and nutrients. Furthermore, PDT induces acute inflammation, attracting leukocytes such as dendritic cells (DCs). PDT might provide a tumor environment that facilitates antigen uptake by DCs and antigen presentation via the MHC class I pathway. As a result, PDT can induce $CD8^+$ cytotoxic T cells, thereby achieving a systemic antitumor effect.

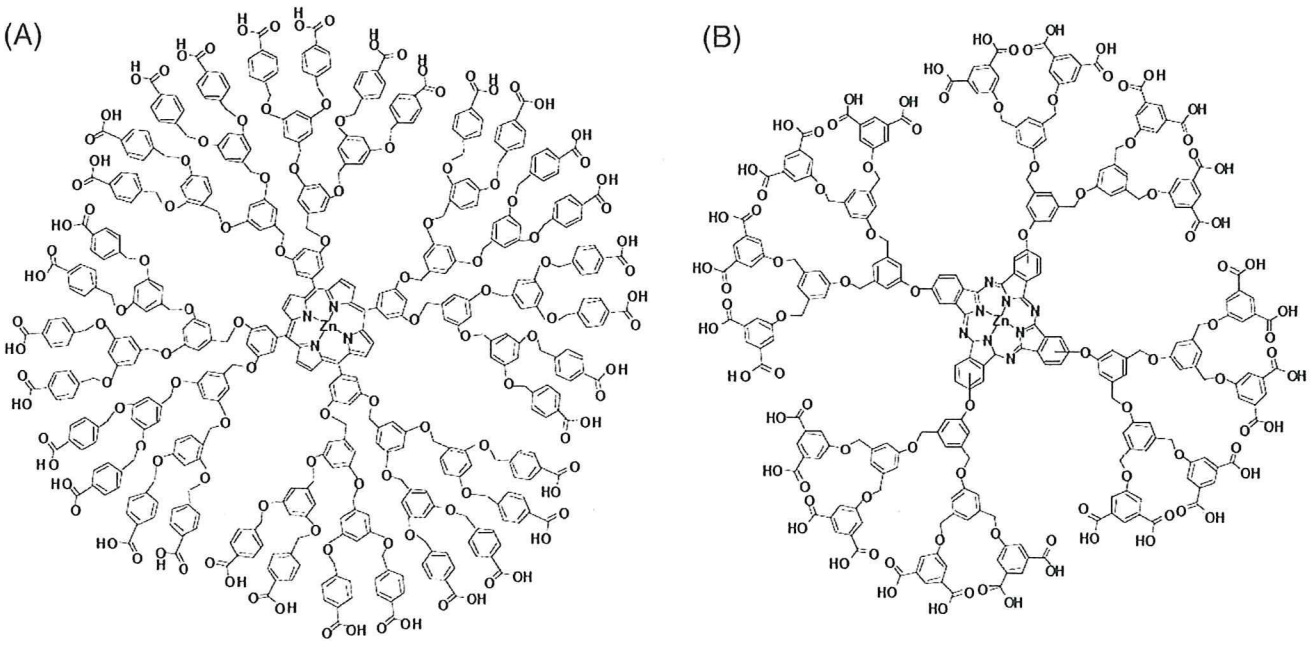

Fig. 3. Chemical structures of ionic dendrimer porphyrin (DP) and ionic dendrimer phthalocyanine (DPc).

The above-mentioned mechanisms indicate the great promise of PDT for use in therapy against malignant tumors. These mechanisms are also very important for the design of nanocarriers for PS delivery. Several key parameters, such as the intratumoral distribution of PSs and modality of cell death, may be controlled by using nanocarriers, which has further motivated us to develop innovative nanocarriers for PDT.

3. Polymeric micelles encapsulating dendrimer photosensitizers for enhanced PDT

3.1. Development of dendrimer photosensitizer-loaded micelles

To date, a number of PSs have been developed and explored in preclinical and clinical studies [1–4]. In general, potent PSs have large π-conjugation domains, such as porphyrin or phthalocyanine rings, that allow them to efficiently absorb energy in the region above 600 nm and a high quantum yield for singlet oxygen formation. Therefore, most PSs easily form aggregates in aqueous media through their π–π stacking and hydrophobic interactions. Such aggregate formation severely decreases ROS formation due to the self-quenching of the excited state [23,43–45]. These properties may hamper the encapsulation into nanocarriers such as liposomes and polymeric micelles. That is, the encapsulation of PSs into nanocarriers might induce the aggregation of PSs, resulting in their reduced PDT efficacy [23]. Also, it is generally difficult to incorporate such very hydrophobic compounds into nanocarriers without compromising the nanocarrier's properties such as the size and surface properties, which are critical to the prolonged blood circulation.

To solve the above-mentioned problems with conventional PSs, we developed ionic dendrimer photosensitizers in which the core of porphyrin or phthalocyanine is surrounded by large dendritic wedges (Fig. 3) [22,29]. It is assumed that dendrimer photosensitizers elicit effective ROS production even at extremely high concentrations, because the dendritic wedges sterically prevent or weaken aggregation of the center dye molecules [20,23]. Also, ionic groups on the dendrimer periphery allow their stable incorporation into polyion complex (PIC) micelles through the electrostatic interaction with oppositely charged poly(ethylene glycol)-polyelectrolyte block

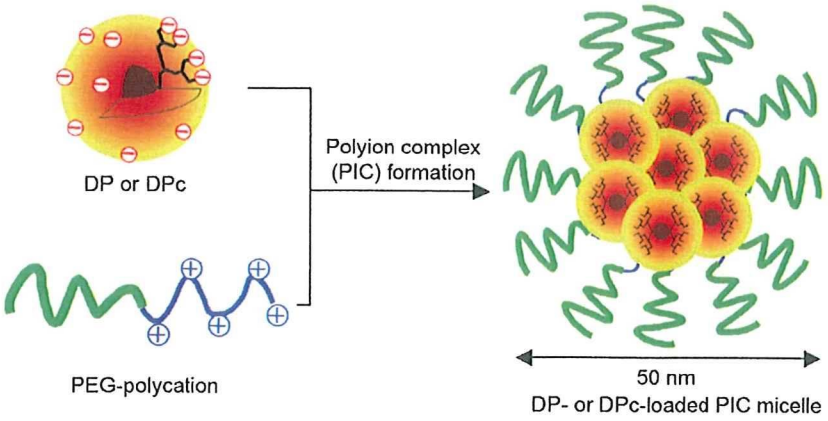

Fig. 4. Formation of DP- or DPc-loaded polyion complex (PIC) micelles through the electrostatic interaction between anionic dendrimers and PEG-polycations. The DP or DPc-loaded micelle is assumed to induce an effective photochemical reaction because the dendritic wedges can sterically prevent or weaken aggregation of the center dye molecules in the micellar core.

Table 1
Physicochemical properties of the DP-loaded micelles from DPs of different generations.

Generation	Hydrodynamic diameter (nm)[a]	Polydispersity index (μ_2/Γ^2)	$M_{w,app}$ (10^5 g/mol)	Association no. PEG-*b*-PLL/DP	CAC[b] (mg/mL)	ζ-potential (mV)
G1	126.5	0.131	2240	8989/32585	<0.1	1.11 ± 0.072
G2	78.0	0.249	100	399/722	<0.1	0.48 ± 0.31
G3	44.0	0.030	9.26	39/38	<0.1	−0.20 ± 0.57

(Reprinted with permission from Ref. [23]. Copyright 2007 by the American Chemical Society).
[a] Cumulant diameter.
[b] Critical association concentration.

copolymers (Fig. 4) [17–24]. Polymeric micelles, which are characterized by a size of several tens of nanometers and a core–shell architecture, are potent nanocarriers for site-specific drug delivery, and several formulations of polymeric micelles containing antitumor agents have progressed to clinical trial [34,46–54].

Recently, we synthesized poly(benzyl ether) dendrimer porphyrins (DPs) with different generations (G*n* = *n*-generation dendrimer, *n* = 1–3) to study the effects of dendritic structure on the formation of PIC micelles and their photochemical properties [23]. Note that DPs have a singlet oxygen quantum yield comparable to protoporphyrin IX, a core constituent PS in DPs, which was measured by direct observation of singlet oxygen luminescence at 1270 nm in MeOD [29]. The PIC micelles (DP-loaded micelles) were prepared by mixing of DPs and poly(ethylene glycol)-poly(L-lysine) block copolymers (PEG-PLL) at a stoichiometric charge ratio, and characterized by dynamic and static light scattering measurements and zeta-potential measurement. As summarized in Table 1, G3 formed narrowly distributed particles with a diameter of 44 nm, which is consistent with the core–shell type micellar structure. On the other hand, G1 and G2 formed relatively larger aggregates with diameters of 126 and 78 nm, respectively. The relatively open architectures and small dendritic wedges of G1 and G2 may not perfectly prevent π–π interactions between DPs, which would account for the large aggregate formation. In regard to the efficiency of the photochemical reactions, we evaluated the fluorescence decay and oxygen consumption ability of DPs in a free or micelle form. The results showed that the G3-loaded micelles showed fluorescence decay and oxygen consumption profiles comparable to those of free G3, whereas the G1- and G2-loaded micelles showed a shortened fluorescence lifetime and decreased oxygen consumption rate compared with free G1 and G2, respectively [23]. It should be noted that the oxygen consumption rate, which was measured by a Clark-type oxygen microelectrode in phosphate-buffered saline containing fetal bovine serum (FBS) as an ROS acceptor, might reflect both the efficiency of ROS formation and the reactivity of the ROS to proteins of FBS [20]. Therefore, the size of dendritic wedges of G3 might be sufficiently large to prevent self-quenching of G3 in the micellar core. This effect contrasts with the fact that conventional PSs easily form aggregates, resulting in decreased ROS formation [23,35–43]. Such aggregate formation and concomitant self-quenching of PSs were also observed when they are incorporated into the liposomes [55,56]. Another important aspect is that the ROS produced from DPs reacted with serum proteins, which are immiscible with PEG chains. We assume that ROS produced in the micellar core may diffuse in the PEG layer and photo-oxidize biomolecules in the solution, although further studies should be performed. In conclusion, we demonstrated that ionic dendrimer photosensitizers with an appropriate dendrimer generation can be efficiently incorporated into polymeric micelles without compromising the efficiency of ROS formation and the reactivity of the ROS to biomolecules.

3.2. In vitro PDT effect of dendrimer photosensitizer-loaded micelles

The in vitro PDT effect (photocytotoxicity) of DPs of different generations (G1, G2 and G3) in a free or micelle form against human cervical adenocarcinoma HeLa cells is shown in Fig. 5. The G1-, G2- and G3-loaded micelles showed 7.5, 50 and 167 times higher photocytotoxicity compared with the corresponding free DPs, respectively. On the other hand, the G1-, G2- and G3-loaded micelles displayed 95, 53 and 15 times higher cellular uptake compared with the corresponding free DPs, respectively. Therefore, the PDT efficiencies, in which the phototoxicity ratio is normalized by the uptake ratio, are calculated to be 0.079, 0.94 and 11.1 for the G1-, G2- and G3-loaded micelles, respectively. The reduced PDT efficiency of the G1-loaded micelle may be responsible for the shortened fluorescence lifetime and decreased oxygen consumption ability. However, the G2-loaded micelle exhibited PDT efficiency comparable to that of free G2 despite the shortened fluorescence lifetime and decreased oxygen consumption. Notably, the G3-loaded micelle showed an 11-fold enhancement in PDT efficiency. We thus made an important observation—i.e., that incorporation of DPs into polymeric micelles enhanced the PDT efficiency [23].

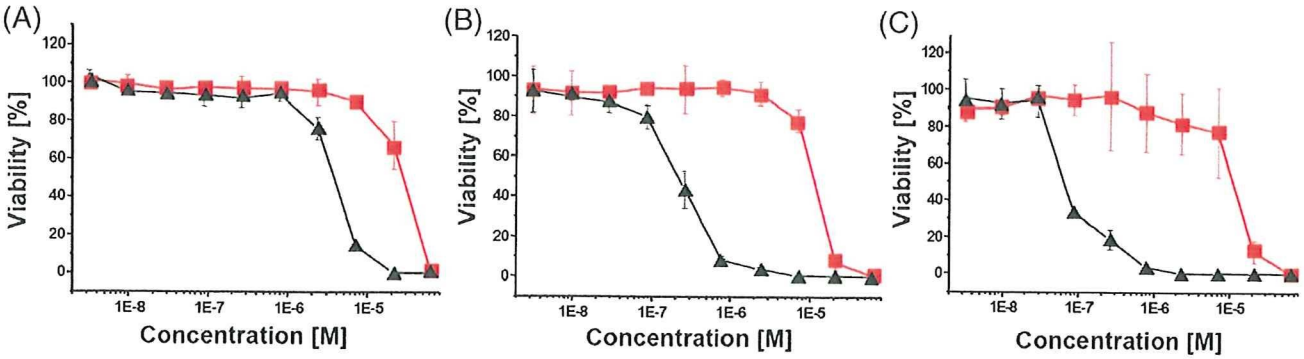

Fig. 5. Cell viability of HeLa cells treated with DPs (red) of different generations [(A): G1, (B): G2 and (C): G3] and the corresponding DP-loaded micelles (black) after photoirradiation. In this experiment, HeLa cells were incubated with DPs or DP-loaded micelles for 12 h, followed by photoirradiation for 30 min with broad-band visible light using a halogen lamp equipped with a filter passing only 400–700 nm light (fluence: 5.4 J cm^{-2}). After 24 h, the cell viability was evaluated by MTT assay. (Reprinted with permission from Ref. [23]. Copyright 2007 by the American Chemical Society).

Table 2
In vitro cytotoxicity of DPc, DPc-loaded micelle and Photofrin after photoirradiation.

Photoirradiation conditions		IC_{50} (μM)[a] of photosensitizing agent		
Time (min)	Fluence (J/cm^2)	DPc	DPc-loaded micelle	Photofrin
0	0	N.D.[b]	N.D.	N.D.
15	2.7	N.D.	1.0	1.0
30	5.4	N.D.	0.20	0.60
45	8.1	N.D.	0.20	0.35
60	10.8	7.0	0.090	0.35

In this experiment, A549 cells were incubated with photosensitizing agents for 12 h, followed by photoirradiation with broad-band visible light using a halogen lamp equipped with a filter passing only 400–700 nm light. After 24 h, the cell viability was evaluated by MTT assay. (Reprinted from Ref. [24]).

[a] 50% cell growth-inhibitory concentration.

[b] IC_{50} was higher than the highest examined concentration (20 μM).

Since in vivo applications of DPs are limited due to their relatively short excitation wavelengths (430 and 559 nm), we also developed an ionic dendrimer phthalocyanine (DPc) with strong Q-band absorption at 685 nm, a wavelength at which the light penetrates deeply into tissues [22]. The simple mixing of DPc and PEG-PLL resulted in the formation of a PIC micelle with a diameter of ca. 50 nm and a narrow size distribution. The photocytotoxicity of the DPc-loaded micelle was assessed against human lung adenocarcinoma A549 cells [24]. Table 2 summarizes the 50% cell growth inhibitory concentrations (IC_{50}) of DPc, the DPc-loaded micelle and clinically used Photofrin. The DPc-loaded micelle showed a fluence-dependent increase in photocytotoxicity, achieving 78 times higher photocytotoxicity than free DPc at 10.8 J/cm^2. It is noted that the DPc-loaded micelle was 3.9 times more effective than Photofrin on a molar basis of photosensitizing units, although the differences in the quantum yields and cellular uptake of photosensitizers were not taken into consideration. Similarly to the above-mentioned DP-loaded micelle, the enhancement of the photocytotoxicity of the DPc-loaded micelle cannot be explained by the intracellular concentration of DPc: the DPc-loaded micelle showed only 7.6 times higher cellular uptake than free DPc. We therefore hypothesize that different mechanisms may be involved in the light-induced cell death between free DPc and DPc-loaded micelle. Indeed, there were appreciable differences in the light-induced morphological changes occurring in the cells treated with IC_{99} of free DPc or DPc-loaded micelle (Fig. 6) [24]. The DPc-loaded micelle induced very rapid cell death accompanied by characteristic morphological changes including swelling and membrane blebbing, whereas free DPc induced gradual shrinkage of the cells. It is noted that the characteristic morphological changes of the cells induced by the DPc-loaded micelle appear to be similar to the characteristics of *oncosis*, which is reported to be induced by several pathological conditions, such as hypoxia, inhibition of ATP production, and increased permeability of the plasma membrane [57]. As shown in Fig. 6, we also monitored the fluorescence of DPc (red) and Rhodamine 123 (Rh123) (green), a dye that specifically stains mitochondria. The fluorescence of DPc became diffusive in both free DPc- and DPc-loaded micelle-treated cells. Since we confirmed that both DPc and the DPc-loaded micelle selectively accumulated in the endo-/lysosomes in separate experiments, the diffused DPc fluorescence in Fig. 6 might indicate that both DPc and the DPc-loaded micelle are translocated from the endo-/lysosomes to the cytoplasm upon photoirradiation. This translocation might arise due to the photochemical disruption of the endo-/lysosomal membranes by photosensitizing agents [58–60]. Indeed, we confirmed that DPc and the DPc-loaded micelle enabled light-induced cytoplasmic delivery of other co-incubated nanocarriers (see Section 5) [60]. In spite of the similar intracellular behaviors between DPc and DPc-loaded micelle, as indicated by the DPc fluorescence, only DPc-loaded micelle caused rapid disappearance of the Rh123 fluorescence in the cell (Fig. 6). This result suggests that the DPc-loaded micelle might affect the mitochondrial functions during photoirradiation. Since the fluorescent intensity of Rh123 is correlated with the amount of ATP in the cells [61], PDT using the DPc-loaded micelle may directly or indirectly clip the ATP in the cell. To determine whether or not the DPc-loaded micelle induces direct photodamage to the mitochondria, we detected the ROS production in the mitochondria by using MitoSOX Red, which rapidly accumulates in the mitochondria and exhibits fluorescence upon oxidation by superoxide and other ROS [24]. As shown in Fig. 7, the DPc-loaded micelle-treated cells displayed apparent fluorescence after 1 min of photoirradiation, whereas the DPc-treated cells showed no fluorescence even after prolonged photoirradiation. Thus, the DPc-loaded micelle was shown to induce photodamage to the mitochondria and thereby affect their functions. In summary, the light-induced cell death caused by the DPc-loaded micelle might involve the following steps (Fig. 8). (i) The DPc-loaded micelle is internalized through endocytosis and accumulates in the endo-/lysosomes. (ii) Upon photoirradiation, the DPc-loaded micelle might escape from the endo-/lysosomes to the cytoplasm by photodamaging the endo-/

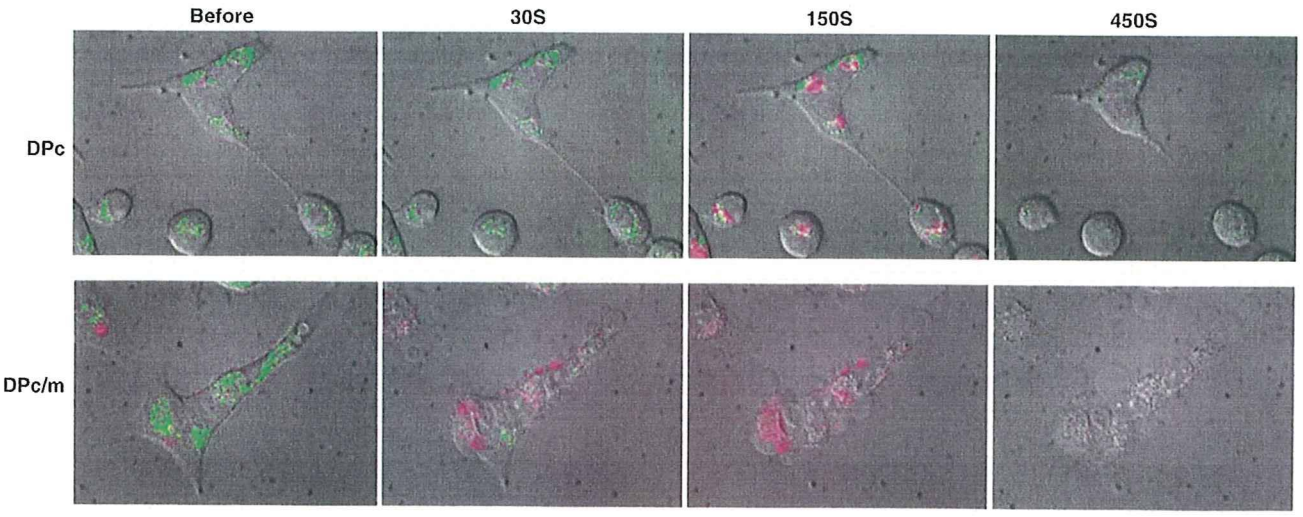

Fig. 6. Time-dependent morphological changes of A549 cells treated with DPc alone or DPc-loaded micelle during photoirradiation. In this experiment, A549 cells were incubated with DPc alone or DPc-loaded micelle for 24 h at a 99% growth inhibitory concentration (IC_{99}). After the medium replacement, the morphological changes in the cells during photoirradiation by the light source of a time-lapse sectioning fluorescent microscope were continuously monitored using the microscope's differential interference contrast (DIC) mode. In addition, the fluorescent images from DPc (red) and Rhodamine 123 (Rh123) (green), a dye that specifically stains mitochondria, were simultaneously monitored. (Reprinted from Ref. [24]).